Journal of Computational Physics 408 (2020) 109238

Contents lists available at ScienceDirect

Journal of Computational Physics

www.elsevier.com/locate/jcp

Optimal, globally constraint-preserving, DG(TD)^2 schemes for computational electrodynamics based on two-derivative Runge-Kutta timestepping and multidimensional generalized Riemann problem solvers – A von Neumann stability analysis

Roger Käppeli [a,d,*], Dinshaw S. Balsara [b], Praveen Chandrashekar [c], Arijit Hazra [c]

[a] Seminar for Applied Mathematics (SAM), Department of Mathematics, ETH Zürich, CH-8092 Zürich, Switzerland
[b] Physics and ACMS Departments, University of Notre Dame, USA
[c] TIFR-Center for Applicable Mathematics, India
[d] Flash Center for Computational Science, Department of Astronomy & Astrophysics, University of Chicago, Chicago, IL 60637, USA

ARTICLE INFO

Article history:
Received 18 July 2019
Received in revised form 28 December 2019
Accepted 29 December 2019
Available online 14 January 2020

Keywords:
Computational electrodynamics
Discontinuous Galerkin
Higher order schemes
Two-derivative Runge-Kutta
Multidimensional generalized Riemann problem solver
von Neumann stability

ABSTRACT

Discontinuous Galerkin (DG) methods have become mainstays in the accurate solution of hyperbolic systems, which suggests that they should also be important for computational electrodynamics (CED). Typically DG schemes are coupled with Runge-Kutta timestepping, resulting in RKDG schemes, which are also sometimes called DGTD schemes in the CED community. However, Maxwell's equations, which are solved in CED codes, have global mimetic constraints. In Balsara and Käppeli [*von Neumann Stability Analysis of Globally Constraint-Preserving DGTD and PNPM Schemes for the Maxwell Equations using Multidimensional Riemann Solvers*, Journal of Computational Physics, 376 (2019) 1108-1137] the authors presented globally constraint-preserving DGTD schemes for CED. The resulting schemes had excellent low dissipation and low dispersion properties. Their one deficiency was that the maximal permissible CFL of DGTD schemes decreased with increasing order of accuracy. The goal of this paper is to show how this deficiency is overcome. Because CED entails the propagation of electromagnetic waves, we would also like to obtain DG schemes for CED that minimize dissipation and dispersion errors even more than the prior generation of DGTD schemes.

Two recent advances make this possible. The first advance, which has been reported elsewhere, is the development of a multidimensional Generalized Riemann Problem (GRP) solver. The second advance relates to the use of Two Derivative Runge Kutta (TDRK) timestepping. This timestepping uses not just the solution of the multidimensional Riemann problem, it also uses the solution of the multidimensional GRP. When these two advances are melded together, we arrive at DG(TD)^2 schemes for CED, where the first "TD" stands for time-derivative and the second "TD" stands for the TDRK timestepping. The *first goal* of this paper is to show how DG(TD)^2 schemes for CED can be formulated with the help of the multidimensional GRP and TDRK timestepping. The *second goal* of this paper is to utilize the free parameters in TDRK timestepping to arrive at DG(TD)^2 schemes for CED that offer a uniformly large CFL with increasing order of accuracy while minimizing the dissipation and dispersion errors to exceptionally low values. The *third goal* of this paper is to document a von Neumann stability analysis of DG(TD)^2 schemes so that their dissipation and dispersion properties can be quantified and studied in detail.

* Corresponding author.
E-mail addresses: roger.kaeppeli@sam.math.ethz.ch (R. Käppeli), dbalsara@nd.edu (D.S. Balsara), praveen@tifrbng.res.in (P. Chandrashekar), arijit@tifrbng.res.in (A. Hazra).

https://doi.org/10.1016/j.jcp.2020.109238

At second order we find a DG(TD)^2 scheme with CFL of 0.25 and improved dissipation and dispersion properties; for a second order scheme. At third order we present a novel DG(TD)^2 scheme with CFL of 0.2571 and improved dissipation and dispersion properties; for a third order scheme. At fourth order we find a DG(TD)^2 scheme with CFL of 0.2322 and improved dissipation and dispersion properties. As an extra benefit, the resulting DG(TD)^2 schemes for CED require fewer synchronization steps on parallel supercomputers than comparable DGTD schemes for CED. We also document some test problems to show that the methods achieve their design accuracy.

1. Introduction

Several areas of science and engineering rely on the accurate, time-dependent computational solution of Maxwell's equations – known as Computational Electrodynamics (CED). The finite-difference time-domain (FDTD) method (Yee [62], Taflove [56], Taflove and Hagness [57], [59], Taflove, Oskooi and Johnson [58]) has been one of the leading methods in CED for over half a century. FDTD relies on the staggering of the variables for the electric and magnetic fields, which provides a direct interpretation of the two curl-type equations given by Faraday's Law and the generalized Ampere's Law. The staggering also naturally satisfies the constraint equations given by Gauss's Laws for electric and magnetic charge, albeit on a staggered pair of control volumes. On a simple Cartesian mesh, every electric field vector component is surrounded by four circulating magnetic field vector components, and every magnetic field vector component is surrounded by four circulating electric field vector components. This compactly staggered arrangement of primal variables is the source of the FDTD method's strength and versatility and allows the method to globally satisfy the divergence constraints. However, it is also important to realize that the FDTD scheme was designed in an era that predates many modern advances in the numerical solution of hyperbolic systems. As a result, many of those advances have not been incorporated in the FDTD algorithm. A very prominent example consists of realizing that the FDTD scheme is restricted to second order of accuracy, especially when spatially varying material properties are involved. In subsequent paragraphs, we take stock of recent advances for hyperbolic systems and their impact on CED, which also enables us to set the goals for this paper.

Maxwell's equations are a hyperbolic system, and there have been significant advances in the numerical solution of hyperbolic systems in the last few decades. Specifically, the higher order Godunov schemes, which were initially formulated at second order, have all been extended to higher orders. The higher order accuracy provides significantly lower dispersion and dissipation in wave propagation, both of which are desirable in CED. The design philosophy underlying higher order Godunov schemes is very general and applies to any hyperbolic system, therefore one expects that they might also apply to CED. Such schemes rely on a detailed analysis of the wave propagation characteristics of a hyperbolic system, and Riemann solvers that contribute to the solution usually encapsulate this information. It is very desirable to incorporate the physics of Riemann solvers into CED schemes (Munz et al. [43], Ismagilov [39], Barbas and Velarde [21]; and references therein) where a set of one dimensional Riemann solvers were worked out for CED. Because these methods are based on finite volume approaches, they are often referred to as finite volume time domain (FVTD) methods. However, in their native form, these FVTD methods for CED do not have the ability to preserve the divergence constraints inherent in Faraday's Law and the generalized Ampere's Law. Discontinuous Galerkin time domain (DGTD) methods provide another approach to attaining high order of accuracy. These DGTD schemes are outgrowths of the original DG methods of Reed and Hill [47], Cockburn & Shu [25], [27], [28], Cockburn, Hou & Shu [26]. While FVTD schemes reconstruct all the higher order moments of the primal variables, DGTD schemes take all these higher order moments and endow them with time-evolution based on the governing equations. Therefore, it is widely believed that increasingly high order DGTD schemes might become almost spectrally accurate in their ability to propagate electromagnetic radiation. Since CED simulates the propagation of electromagnetic waves, it is believed that higher order DGTD schemes might be well-suited to CED. However, previous generations of DGTD schemes for CED were not globally constraint-preserving (Hesthaven and Warburton [37], Cockburn, Li and Shu [29] Kretzschmar et al. [40], Egger et al. [32], Bokil et al. [22], Chen and Liu [24]; Ren et al. [48]; Wang et al. [60]; Sun et al. [55], Angulo et al. [1]). We see, therefore, that classical FVTD and DGTD schemes cannot be naïvely extended to have all the constraint-preserving advantages for FDTD.

The picture begins to become clearer when one starts looking at recent advances in numerical magnetohydrodynamics (MHD). The MHD equations consist of Faraday's law for the evolution of the magnetic field coupled to the usual hydrodynamic equations with additional forces resulting from the Lorentz force law. Just like CED, Faraday's law in MHD simulations has to be evolved in time in a mimetic, constraint-preserving fashion. As a result, two important advances had to be introduced in numerical MHD, which carry over quite naturally to CED. In the next paragraph we explain how those advances were originated in MHD; the paragraph after that will explain how they have been extended to CED.

In order to have a mimetic scheme for MHD, the magnetic field components are collocated at the faces of the mesh, while the electric field components are collocated at the edges of the mesh. This gives the same Yee-scheme type staggering of variables that is also used to advantage in FDTD schemes for CED. However, the fluid variables are collocated at the zone centers and can be reconstructed over the volume of each zone, as is traditionally done in any higher order Godunov

scheme. The facially-collocated magnetic field variables then have to be reconstructed for each zone just like the fluid variables. A constraint-preserving reconstruction strategy was crucial to starting with the facial magnetic field components and making a high order representation of the magnetic field available throughout the zone. This reconstruction strategy, which is consistent with the constraint from Gauss' law for magnetic fields, was presented in Balsara [2], [3], [4], Balsara and Dumbser [9], Xu et al. [63], Balsara et al. [13]. It ensures that the magnetic field is available over the same volume as the fluid flow variables. Once the magnetic field and flow variables are available within each volume, we wish to find the electric field variables at each edge of the mesh. However, at each edge of a Cartesian mesh, we will have four sets of MHD variables, one from each of the four zones that surround that edge. The only way to obtain the unique electric field associated with the edge under consideration is via a multidimensional Riemann solver. Such multidimensional Riemann solvers were formulated by Balsara [5], [6], [8], [11], Balsara, Dumbser and Abgrall [7], Balsara and Dumbser [10], Balsara et al. [12], Balsara and Nkonga [17]. Using these twin advances of a constraint-preserving reconstruction of the magnetic field and the multidimensional Riemann solver, Balsara and Käppeli [14] were able to formulate a mimetic DGTD scheme for MHD.

In a sequence of recent papers (Balsara et al. [13], [15], [16]) the above-mentioned advances have also been extended to design constraint-preserving, higher order Godunov, FVTD schemes for CED. (These FVTD schemes also benefited from the ADER time discretization of Dumbser et al. [31].) Globally constraint-preserving DGTD schemes for CED were also formulated by Balsara and Käppeli [18]. Hazra et al. [36] have also implemented such DGTD schemes and shown them to work with their design accuracies even for problems that have strong variation in material properties. Therefore, a basic goal was achieved, i.e. one had access to a fully constraint-preserving DGTD scheme for CED with its attendant spectral-like accuracies that could work at up to fifth order of accuracy even in the presence of spatially varying permittivity and permeability. The higher order schemes in the DGTD family also show diminishing dissipation and improved dispersion with increasing order; which is a very salutary sign. However, the resulting schemes showed the same trend that we see in all DG schemes – i.e., the timestep reduces as the order of accuracy of the DG scheme is increased. Two recent advances make it possible to improve on the already very accurate family of DGTD schemes. First, it has become possible to modify the timestepping strategy so as to reduce the dissipation and improve the CFL number. Second, a novel generation of multidimensional generalized Riemann problem (GRP) solvers have been designed which make it feasible to implement the above-mentioned timestepping strategies. The overarching goal of this paper is to document the first of these two advances and show how it opens the door to improved DGTD schemes with large time steps and low dissipation and dispersion for CED. The second of these two advances has already been documented in Balsara et al. [20].

Traditionally, in numerical work for hyperbolic PDEs, strong stability preserving Runge-Kutta (SSP-RK) schemes have been used for the time-evolution of hyperbolic systems. Such schemes (Shu and Osher [52], [53], [54], Spiteri and Ruuth [50], [51], Gottlieb et al. [34]) try to reduce the total variation in the solution at the end of a timestep. They are very useful for non-linear hyperbolic systems, where the presence of shocks can otherwise cause the total variation in the solution to increase. However, the time update of linear systems like CED does not necessarily mandate the strong stability preserving property. Instead, for CED, the optimal time-evolution strategies should lower the dispersion and dissipation of the numerical scheme while simultaneously enabling a large timestep. This encourages us to seek alternative timestepping strategies which are more suited to linear systems. A very interesting class of methods for integrating ordinary differential equations (ODEs) with high order of accuracy was presented in Chan and Tsai [23]. Those authors realized that for ODEs of the form $y' = f(y)$ it is sometimes very inexpensive to additionally evaluate the second derivative $y'' = g(y) \equiv f'(y) f(y)$. In other words, by incorporating the second derivative into the update strategy one can obtain a scheme with fewer stages and higher order of accuracy per stage. Chan and Tsai [23] called their schemes two-derivative Runge-Kutta (TDRK) schemes. Grant et al. [35] then extended this idea to arrive at what they call SSP-TS (Strong Stability Preserving – Taylor Series) schemes for the time-update of non-linear hyperbolic systems.

It should be noted that the SSP-TS schemes of Grant et al. [35] are, in some sense, abstract constructions because those authors do not give us much guidance on how the time-derivative of a numerical flux is to be obtained. Without a practical, implementable, strategy for obtaining that time-derivative, an SSP-TS scheme is not very useful. Indeed, the only examples that Grant et al. [35] show in their paper are nominal ones. In another line of inquiry, Balsara and his co-workers were developing generalized Riemann problem (GRP) solvers. Such GRP solvers can be applied to any hyperbolic system and they indeed provide an implementable approach for obtaining the time-derivative of a numerical flux. The GRP solvers, therefore, make it feasible to design SSP-TS schemes for any hyperbolic system. In Goetz et al. [33] and Balsara et al. [19] we presented this novel class of one-dimensional GRP solvers which are capable of making SSP-TS schemes practicable. However, please realize that FVTD and DGTD schemes for CED require multidimensional Riemann solvers; therefore, TDRK-based DGTD schemes for CED require the existence of multidimensional GRP solvers. This milestone was breached in Balsara et al. [20]. It opens the door to TDRK-based DGTD schemes for CED. The *first goal* of this paper is to formulate TDRK-based DGTD schemes. (In Balsara et al. [20] we only documented TDRK-based FVTD schemes because the design of TDRK-based DGTD schemes was deemed to be too much of a challenge to be breached in one paper.) We refer to the novel schemes for CED by the compact name of DG(TD)^2 schemes because the first "TD" stands for time-derivative and the second "TD" stands for the TDRK timestepping.

The SSP-TS schemes have a strong stability preserving property but use a Taylor series expansion (i.e. a second derivative evaluation) in the time-update strategy. However, for a linear hyperbolic system like CED, the SSP property is not truly needed. On the other hand, some desirable properties like low dispersion, low dissipation and robust CFL are highly desired.

Therefore, the *second goal* of this paper is to utilize all the free parameters in TDRK timestepping to arrive at DG(TD)^2 schemes for CED that optimize the desirable features mentioned above. Such attempts to obtain low dissipation and low dispersion schemes has indeed been attempted within the context of Runge-Kutta timestepping (Hesthaven and Warburton [38], Sarmany et al. [49], Diehl et al. [30], Niegemann et al. [44], Williamson [61]). However, it has never been attempted within the context of TDRK schemes.

Prior work on DG schemes has shown that there are several very valuable insights to be gained by analyzing the stability of such schemes (Liu et al. [42], Zhang and Shu [65], Yang and Li [64], Balsara and Käppeli [14], [18]). As the *third goal* this paper, we document a von Neumann stability analysis of DG(TD)^2 schemes for CED which have low dissipation and dispersion while permitting a robust timestep. In a subsequent paper we will document practical, fully-working DG(TD)^2 schemes for CED which work with spatially varying material properties.

In Section 2 we introduce the Two Derivative Runge-Kutta (TDRK) timestepping and identify the free parameters that will be used in the ensuing optimization study. In Section 3 we explain how DG(TD)^2 schemes are obtained from their DGTD predecessors. A von Neumann stability analysis of second order DG(TD)^2 schemes reveals that they have several very desirable properties that should be developed at higher orders. In Section 4 we show how the two-stage TDRK timestepping can be optimized to yield improved third order DG(TD)^2 schemes for CED. In Section 5 we show how the three-stage TDRK timestepping can be optimized to yield improved fourth order DG(TD)^2 schemes for CED. Von Neumann stability analyses for the optimized third and fourth order DG(TD)^2 schemes for CED are also presented in Sections 4 and 5 respectively.

2. Description of two derivative Runge-Kutta (TDRK) timestepping

Consider the PDE that is formally written as

$$\frac{\partial \mathbf{U}}{\partial t} = \mathbf{F}(\mathbf{U}) \tag{2.1}$$

where $\mathbf{U}$ is a vector of M components and $\mathbf{F}(\mathbf{U})$ is negative of the gradient of the fluxes. We assume that a suitable GRP solver is available which provides $\dot{\mathbf{F}}(\mathbf{U})$, which is the time-derivative of $\mathbf{F}(\mathbf{U})$. (The GRP solver takes as its inputs not just the states that are usually sent into a Riemann solver but also the multidimensional gradients of those states. It produces as its output, not just the fluxes but also the time derivatives of the fluxes.) The time-explicit two-derivative RK schemes with "s" internal stages can be written as

$$\begin{aligned}
\mathbf{U}^{(i)} &= \mathbf{U}^n + \Delta t \sum_{j=1}^{i-1} a_{ij} \mathbf{F}\left(\mathbf{U}^{(j)}\right) + \Delta t^2 \sum_{j=1}^{i-1} \hat{a}_{ij} \dot{\mathbf{F}}\left(\mathbf{U}^{(j)}\right), \quad i = 2, ..., s \\
\mathbf{U}^{n+1} &= \mathbf{U}^n + \Delta t \sum_{j=1}^{s} b_j \mathbf{F}\left(\mathbf{U}^{(j)}\right) + \Delta t^2 \sum_{j=1}^{s} \hat{b}_j \dot{\mathbf{F}}\left(\mathbf{U}^{(j)}\right)
\end{aligned} \tag{2.2}$$

where we start the timestep with $\mathbf{U}^{(1)} = \mathbf{U}^n$ and the above timestepping scheme enables us to evolve the solution $\mathbf{U}^n$ at time t^n to a solution $\mathbf{U}^{n+1}$ at time $t^{n+1} = t^n + \Delta t$. We now document the two-stage and three-stage schemes in their own sections and identify the parameters that can be optimized.

2.1. Two-stage TDRK scheme

The two-stage TDRK scheme that can be up to fourth order accurate in time is written as

$$\begin{aligned}
\mathbf{U}^* &= \mathbf{U}^n + \Delta t a_{21} \mathbf{F}\left(\mathbf{U}^n\right) + \Delta t^2 \hat{a}_{21} \dot{\mathbf{F}}\left(\mathbf{U}^n\right) \\
\mathbf{U}^{n+1} &= \mathbf{U}^n + \Delta t \left[b_1 \mathbf{F}\left(\mathbf{U}^n\right) + b_2 \mathbf{F}\left(\mathbf{U}^*\right)\right] + \Delta t^2 \left[\hat{b}_1 \dot{\mathbf{F}}\left(\mathbf{U}^n\right) + \hat{b}_2 \dot{\mathbf{F}}\left(\mathbf{U}^*\right)\right]
\end{aligned} \tag{2.3}$$

The condition for ensuring first order of accuracy is

$$b_1 + b_2 = 1 \tag{2.4}$$

The condition for ensuring second order of accuracy is

$$b_2 a_{21} + \hat{b}_1 + \hat{b}_2 = \frac{1}{2} \tag{2.5}$$

The conditions for ensuring third order of accuracy are

$$b_2 a_{21}^2 + 2\hat{b}_2 a_{21} = \frac{1}{3}; \quad b_2 \hat{a}_{21} + \hat{b}_2 a_{21} = \frac{1}{6} \tag{2.6}$$

The conditions for ensuring fourth order accuracy are

$$b_2 a_{21}^3 + 3\hat{b}_2 a_{21}^2 = \frac{1}{4}; \quad b_2 a_{21}\hat{a}_{21} + \hat{b}_2 a_{21}^2 + \hat{b}_2 \hat{a}_{21} = \frac{1}{8}; \quad \hat{b}_2 a_{21}^2 = \frac{1}{12}; \quad \hat{b}_2 \hat{a}_{21} = \frac{1}{24} \tag{2.7}$$

If all of the above conditions are satisfied, the TDRK scheme in Eq. (2.3) becomes fourth order accurate. The unique choice of parameters that give rise to full fourth order of accuracy is given by Chan and Tsai [23]

$$b_1 = 1; \quad b_2 = 0; \quad \hat{b}_1 = \frac{1}{6}; \quad \hat{b}_2 = \frac{1}{3}; \quad a_{21} = \frac{1}{2}; \quad \hat{a}_{21} = \frac{1}{8} \tag{2.8}$$

Of course, we have the option of settling for lower than fourth order of accuracy as long as the resultant scheme gives us some other very desirable features. In other words, if the spatial accuracy is just third order, we do not object to a temporal accuracy that is also restricted to third order as long as we get some additional nice attributes in our numerical method. We explore that next.

We realize from Eqs. (2.4), (2.5), (2.6) and (2.7) that only the first three of those four equations are needed in order to ensure third order accuracy. Therefore, two of the six coefficients in Eq. (2.3) for the time update are indeed free. We realize that the process of choosing which two coefficients to pick is not unique. However, we pick $\hat{b}_2 \to u_1$ and $a_{21} \to u_2$. With this choice, Eqs. (2.4), (2.5) and (2.6) uniquely allow us to identify the rest of the four coefficients as

$$b_1 = \frac{3u_2^2 + 6u_1u_2 - 1}{3u_2^2}; \quad b_2 = \frac{6u_1u_2 - 1}{3u_2^2}; \quad \hat{b}_1 = \frac{6u_1u_2 + 3u_2 - 2}{6u_2}; \quad \hat{a}_{21} = \frac{u_2^2}{2} \tag{2.9}$$

We see, therefore, that within a two-stage TDRK scheme there is the freedom to optimize a scheme that is third order accurate in space and time. We can, therefore, make a two-parameter plot in (u_1, u_2) space where we plot out one or the other desirable feature. We can also plot out multiple such features. For example, we might prioritize the process of obtaining the largest CFL but we may additionally want to minimize the dissipation or dispersion so that they lie below certain thresholds. We can then use such machine-generated plots to identify for us the regions in the two-parameter (u_1, u_2) space where we may expect good performance of the resultant scheme. The last step could possibly involve a human being who could identify schemes that meet certain criteria of excellence that a computationalist may subjectively want in his/her schemes.

2.2. Three-stage TDRK scheme

The three-stage TDRK scheme that can be up to sixth order accurate in time is written as

$$\begin{aligned}
\mathbf{U}^* &= \mathbf{U}^n + \Delta t a_{21}\mathbf{F}\left(\mathbf{U}^n\right) + \Delta t^2 \hat{a}_{21}\dot{\mathbf{F}}\left(\mathbf{U}^n\right) \\
\mathbf{U}^{**} &= \mathbf{U}^n + \Delta t\left[a_{31}\mathbf{F}\left(\mathbf{U}^n\right) + a_{32}\mathbf{F}\left(\mathbf{U}^*\right)\right] + \Delta t^2\left[\hat{a}_{31}\dot{\mathbf{F}}\left(\mathbf{U}^n\right) + \hat{a}_{32}\dot{\mathbf{F}}\left(\mathbf{U}^*\right)\right] \\
\mathbf{U}^{n+1} &= \mathbf{U}^n + \Delta t\left[b_1\mathbf{F}\left(\mathbf{U}^n\right) + b_2\mathbf{F}\left(\mathbf{U}^*\right) + b_3\mathbf{F}\left(\mathbf{U}^{**}\right)\right] + \Delta t^2\left[\hat{b}_1\dot{\mathbf{F}}\left(\mathbf{U}^n\right) + \hat{b}_2\dot{\mathbf{F}}\left(\mathbf{U}^*\right) + \hat{b}_3\dot{\mathbf{F}}\left(\mathbf{U}^{**}\right)\right]
\end{aligned} \tag{2.10}$$

The condition for ensuring first order of accuracy is

$$b_3 + b_2 + b_1 = 1 \tag{2.11}$$

The condition for ensuring second order of accuracy is

$$b_2 a_{21} + \hat{b}_1 + \hat{b}_2 + \hat{b}_3 + b_3\left(a_{32} + a_{31}\right) = \frac{1}{2} \tag{2.12}$$

The conditions for ensuring third order of accuracy are

$$\begin{aligned}
&b_2 a_{21}^2 + 2\hat{b}_2 a_{21} + b_3\left(a_{31} + a_{32}\right)^2 + 2\hat{b}_3\left(a_{31} + a_{32}\right) = \frac{1}{3}; \\
&b_2\hat{a}_{21} + \hat{b}_2 a_{21} + b_3\left(\hat{a}_{31} + \hat{a}_{32} + a_{21}a_{32}\right) + \hat{b}_3\left(a_{31} + a_{32}\right) = \frac{1}{6}
\end{aligned} \tag{2.13}$$

The conditions for ensuring fourth order accuracy are

$$\begin{aligned}
&b_2 a_{21}^3 + 3\hat{b}_2 a_{21}^2 + b_3\left(a_{31} + a_{32}\right)^3 + 3\hat{b}_3\left(a_{31} + a_{32}\right)^2 = \frac{1}{4} \\
&b_2 a_{21}\hat{a}_{21} + \hat{b}_2 a_{21}^2 + \hat{b}_2\hat{a}_{21} + b_3 a_{21}a_{32}\left(a_{31} + a_{32}\right) + b_3\left(a_{31} + a_{32}\right)\left(\hat{a}_{31} + \hat{a}_{32}\right) \\
&\qquad + \hat{b}_3 a_{21}a_{32} + \hat{b}_3\left(a_{31} + a_{32}\right)^2 + \hat{b}_3\left(\hat{a}_{31} + \hat{a}_{32}\right) = \frac{1}{8} \\
&\hat{b}_2 a_{21}^2 + b_3 a_{21}^2 a_{32} + 2b_3 a_{21}\hat{a}_{32} + \hat{b}_3\left(a_{31} + a_{32}\right)^2 = \frac{1}{12} \\
&\hat{b}_2\hat{a}_{21} + b_3 a_{21}\hat{a}_{32} + b_3 a_{32}\hat{a}_{21} + \hat{b}_3 a_{21}a_{32} + \hat{b}_3\left(\hat{a}_{31} + \hat{a}_{32}\right) = \frac{1}{24}
\end{aligned} \tag{2.14}$$

The conditions for ensuring fifth and sixth order of accuracy are documented in the appendix of Grant et al. [35]. They are not very relevant to the discussion of this paper which is why we do not document them here. Eqs. (2.11), (2.12), (2.13) and (2.14) represent eight conditions for the twelve coefficients of the three-stage TDRK scheme. Hence, we realize that we have four degrees of freedom available for the optimization.

3. Obtaining DG(TD)^2 schemes from their DGTD predecessors

We consider a simplified set of CED equations for the following von Neumann stability analysis. We assume that the permittivity ε and permittivity μ are simple scalars with no spatial variation. Furthermore, we assume vanishing current and charge densities. That is the usual level of simplification that is used in the CED field when carrying out a von Neumann stability analysis. The corresponding form of the extended Ampère's law for the evolution of the electric displacement field $\mathbf{D}$ reads

$$\frac{\partial \mathbf{D}}{\partial t} - \frac{1}{\mu}\nabla \times \mathbf{B} = 0. \tag{3.1}$$

Likewise, Faraday's law for the evolution of the magnetic induction $\mathbf{B}$ reads

$$\frac{\partial \mathbf{B}}{\partial t} + \frac{1}{\varepsilon}\nabla \times \mathbf{D} = 0. \tag{3.2}$$

Both fields are subject to the involution constraints

$$\nabla \cdot \mathbf{B} = 0 \quad \text{and} \quad \nabla \cdot \mathbf{D} = 0. \tag{3.3}$$

As Balsara and Käppeli [18], we introduce one further simplification by assuming that all significant variations are restricted to the two-dimensional xy-plane. We focus on the transverse electric TE$_z$ mode by letting the z-component of the electric displacement field $\mathbf{D}$ and the x- and y-components of the magnetic induction $\mathbf{B}$ vanish. We remark that we could as well analyze the transverse magnetic TM$_z$ mode due the symmetry properties of the DGTD and DG(TD)^2 schemes (see Balsara and Käppeli [18]). The CED equations can then be written in the compact form

$$\frac{\partial}{\partial t}\begin{pmatrix} D_x \\ D_y \\ B_z \end{pmatrix} + \frac{\partial}{\partial x}\begin{pmatrix} 0 \\ B_z/\mu \\ D_y/\varepsilon \end{pmatrix} + \frac{\partial}{\partial y}\begin{pmatrix} -B_z/\mu \\ 0 \\ -D_x/\varepsilon \end{pmatrix} = 0. \tag{3.4}$$

These are the simplified equations for which we will develop the DG(TD)^2 schemes below. We stress that this restriction to a two-dimensional Cartesian setting is done for the technical feasibility of the von Neumann stability analysis below. The DG(TD)^2 schemes would in principle be generalizable to three dimensions and the practically relevant unstructured meshes. However, this would be beyond the scope of the present publication.

In the rest of the section, we show how the DGTD schemes that were documented in Sections 3 and 4 of Balsara and Käppeli [18] can now be extended to yield DG(TD)^2 schemes. We only need to demonstrate this for second order because the process becomes self-evident after that. This extension is shown in Sub-section 3.1. In Sub-section 3.2 we present the von Neumann stability analysis for such a second order DG(TD)^2 scheme, showing that it results in a scheme with dissipation and dispersion that are an improvement over those of a DGTD scheme with SSP-RK timestepping.

3.1. Second order single-stage DG(TD)^2 scheme obtained from second order two stage DGTD scheme

We start by pointing out that the DGTD and the here presented DG(TD)^2 schemes are not traditional DG schemes for conservation laws due to the curl-type CED equations and their constraint-preservation properties. Therefore, we call them DG-like schemes. We refer to Section II of Balsara and Käppeli [14] for a detailed comparison between the DG-like schemes and a traditional DG scheme.

Although we are interested in two-dimensional schemes, we begin by outlining the schemes on a three-dimensional mesh. This is important to appreciate the constraint-preserving DG-like formulation. The restriction to two dimensions and the TE$_z$ mode follows then easily. One computational zone of a uniform Cartesian three-dimensional mesh with zone widths Δx, Δy, Δz is shown in Fig. 1. The zone spans the domain $[-\Delta x/2, +\Delta x/2] \times [-\Delta y/2, +\Delta y/2] \times [-\Delta z/2, +\Delta z/2]$. Let $\hat{\mathbf{n}}$ be the unit outward pointing normal of a face (of the considered zone) and A_n be the face's area. Concretely, say we take the right x-face in Fig. 1 that contains the field component D_x we wish to evolve with Eq. (3.1). Then $\hat{\mathbf{n}} = \hat{\mathbf{x}}$ and $A_n = \Delta y \Delta z$ is the area of the face. Now say we take the upper y-face in Fig. 1 that contains the field component D_y we wish to evolve with Eq. (3.1). Then $\hat{\mathbf{n}} = \hat{\mathbf{y}}$ and $A_n = \Delta x \Delta z$ is the area of the face. In order to find the evolution equations for the field components, we project Eq. (3.1) into a space of test functions. The test functions will be identical to the trial functions and will be made explicit below. To make the DG-like projection, we first multiply the extended Ampère's law Eq. (3.1) with a test function ϕ. Then we restrict the attention to the face A_n by taking the scalar product with the unit normal $\hat{\mathbf{n}}$ of that face. Next, we integrate over the considered face to get

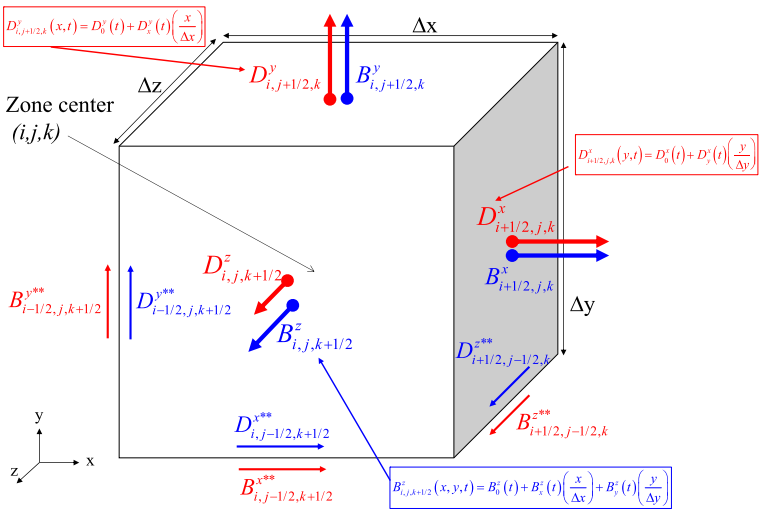

Fig. 1. Shows us that the primal variables of the DG scheme, given by the normal components and their higher moments for the magnetic induction and electric displacement field. These variables are facially-collocated and are explicitly shown in the figure for the two-dimensional second order accurate DG scheme. They undergo an update from Faraday's law and the generalized Ampere's law respectively. The components of the primal magnetic induction vector and its higher moments are shown by the thick blue arrows while the components of the primal electric displacement vector and its higher moments are shown by the thick red arrows. The edge-collocated electric displacement fields, which are used for updating the facial magnetic induction components, are shown by the thin blue arrows close to the appropriate edge. The edge-collocated magnetic induction fields, which are used for updating the facial electric displacement components, are shown by the thin red arrows close to the appropriate edge. (For interpretation of the references to color in this figure, the reader is referred to the web version of this article.)

$$\frac{\partial}{\partial t}\left(\int_{A_n}\left(\hat{\mathbf{n}}\cdot\mathbf{D}\right)\phi dA_n\right)-\frac{1}{\mu}\int_{\partial A_n}(\phi\mathbf{B})\cdot d\mathbf{l}+\frac{1}{\mu}\int_{A_n}\hat{\mathbf{n}}\cdot[(\nabla\phi)\times\mathbf{B}]dA_n=0 \tag{3.5}$$

where the elementary vector identity

$$\nabla\times(\phi\mathbf{D})=(\nabla\phi)\times\mathbf{D}+\phi\nabla\times\mathbf{D} \tag{3.6}$$

and Stokes' theorem were used. The boundary of the face is denoted by ∂A_n and the infinitesimal line element by $d\mathbf{l}$. Eqn. (3.5) is the desired Galerkin projection applied to Ampère's law Eq. (3.1) (a curl-type equation) at a face of the mesh. The second term is a numerical flux integrated along the edges of the face under consideration. Realize that at the edges, four states (from four neighboring zones) come together. This requires the usage of a multidimensional Riemann solver. (Note that this is also the case in a two-dimensional setting when a z-edge collapses to a vertex in the xy-plane.) This term is analogous to the numerical flux term in a traditional DG scheme. The third term is an integral over the face and it is analogous to the volume term in a traditional DG scheme.

Along the same lines, one derives a Galerkin projection applied to Faraday's law Eq. (3.2) at a face of the mesh:

$$\frac{\partial}{\partial t}\left(\int_{A_n}\left(\hat{\mathbf{n}}\cdot\mathbf{B}\right)\phi dA_n\right)+\frac{1}{\varepsilon}\int_{\partial A_n}(\phi\mathbf{D})\cdot d\vec{\ell}-\frac{1}{\varepsilon}\int_{A_n}\hat{\mathbf{n}}\cdot[(\nabla\phi)\times\mathbf{D}]dA_n=0. \tag{3.7}$$

Next, we specialize the discussion to the here relevant two-dimensional case by suppressing any variation in the z-direction.

From Fig. 1, we see that the second order accurate representation of the x-component of the displacement vector at $x=\Delta x/2$ is given by

$$D^x(y,t)=D_0^x(t)+D_y^x(t)\left(\frac{y}{\Delta y}\right). \tag{3.8}$$

The trial functions are $\phi(y)=1$ and $\phi(y)=(y/\Delta y)$, i.e. the zeroth and first orthogonal Legendre polynomials over the interval $[-\Delta y/2,\ +\Delta y/2]$. Similarly, the second order accurate representation of the y-component of the displacement vector at $y=\Delta y/2$ is given by

$$D^y(x,t)=D_0^y(t)+D_x^y(t)\left(\frac{x}{\Delta x}\right). \tag{3.9}$$

The trial functions are $\phi(x)=1$ and $\phi(x)=(x/\Delta x)$, i.e. the zeroth and first orthogonal Legendre polynomials over the interval $[-\Delta x/2,\ +\Delta x/2]$. In like fashion, the second order accurate representation of the z-component of the magnetic induction vector is represented in the xy-plane as

$$B^z(x,y,t) = B_0^z(t) + B_x^z(t)\left(\frac{x}{\Delta x}\right) + B_y^z(t)\left(\frac{y}{\Delta y}\right). \tag{3.10}$$

The trial functions are $\phi(x,y)=1$, $\phi(x,y)=(x/\Delta x)$ and $\phi(x,y)=(y/\Delta y)$, i.e. orthogonal Legendre polynomials over $[-\Delta x/2,+\Delta x/2]\times[-\Delta y/2,+\Delta y/2]$. Observe that in keeping with the philosophy for Discontinuous Galerkin schemes, all the modes/trial functions in the above three equations have been endowed with time-dependence. This ensures that as the order of accuracy is increased, the DG schemes approach spectral accuracy.

The evolution equations for the modes of the x-component of the displacement vector at $x=\Delta x/2$ are then obtained by instantiating Eq. (3.5). With $\hat{\mathbf{n}}=\hat{\mathbf{x}}$ and the test function $\phi(y)=1$, Eq. (3.5) gives us

$$\frac{dD_0^x(t)}{dt} = \frac{1}{\mu}\frac{1}{\Delta y}\left[B^{z^{**}}(x=\Delta x/2, y=\Delta y/2) - B^{z^{**}}(x=\Delta x/2, y=-\Delta y/2)\right]. \tag{3.11a}$$

Likewise, with $\hat{\mathbf{n}}=\hat{\mathbf{x}}$ and the test function $\phi(y)=(y/\Delta y)$ in Eq. (3.5) we get

$$\begin{aligned}\frac{dD_y^x(t)}{dt} = \frac{1}{\mu}\frac{6}{\Delta y}&\left[B^{z^{**}}(x=\Delta x/2, y=\Delta y/2) + B^{z^{**}}(x=\Delta x/2, y=-\Delta y/2)\right]\\ &-\frac{1}{\mu}\frac{12}{\Delta y}\left\langle B^{z^{*}}(x=\Delta x/2, y)\right\rangle\end{aligned} \tag{3.11b}$$

Here $B^{z^{**}}(x=\Delta x/2, y=\Delta y/2)$ and $B^{z^{**}}(x=\Delta x/2, y=-\Delta y/2)$ are magnetic induction components that are obtained at the two endpoints of the right x-face. They are obtained by the application of a two-dimensional Riemann solver at the edges of the mesh (explicit expressions are given below). Also notice that the terms within angled brackets $\langle\rangle$, represent suitably high order line averages within a face, i.e.

$$\left\langle B^{z^{*}}(x=\Delta x/2, y)\right\rangle = \frac{1}{\Delta y}\int_{-\Delta y/2}^{+\Delta y/2} B^{z^{*}}(x=\Delta x/2, y)\,dy.$$

These terms with an angled bracket are to be obtained with a suitably high order quadrature over each face of the mesh. In this work, since the z-variation is suppressed, we use the well-known one-dimensional Gauss-Legendre quadrature to carry out the facial integrals. One-dimensional Riemann problems in the right face being considered will furnish the $B^{z^{*}}(x=\Delta x/2, y)$ component of the magnetic induction field that is to be used in the angled brackets. These Riemann problems are solved at each of the quadrature points in the x-face. Let the two states have subscripts L (for left) and R (for right). Then $B^{z^{*}}(x=\Delta x/2, y)$ is given explicitly by

$$B^{z^{*}} = \frac{1}{2}\left(B_L^z + B_R^z\right) - \frac{1}{2c}\left(D_R^y/\varepsilon - D_L^y/\varepsilon\right). \tag{3.12}$$

The evolution equations for the modes of the y-component of the displacement vector at $y=\Delta y/2$ are obtained by instantiating Eq. (3.5). Using $\hat{\mathbf{n}}=\hat{\mathbf{y}}$ and the test function $\phi(x)=1$, Eq. (3.5) then gives us

$$\frac{dD_0^y(t)}{dt} = -\frac{1}{\mu}\frac{1}{\Delta x}\left[B^{z^{**}}(x=\Delta x/2, y=\Delta y/2) - B^{z^{**}}(x=-\Delta x/2, y=\Delta y/2)\right]. \tag{3.13a}$$

With $\hat{\mathbf{n}}=\hat{\mathbf{y}}$ and the test function $\phi(x)=(x/\Delta x)$ in Eq. (3.5) we get

$$\begin{aligned}\frac{dD_x^y(t)}{dt} = -\frac{1}{\mu}\frac{6}{\Delta x}&\left[B^{z^{**}}(x=\Delta x/2, y=\Delta y/2) + B^{z^{**}}(x=-\Delta x/2, y=\Delta y/2)\right]\\ &+\frac{1}{\mu}\frac{12}{\Delta x}\left\langle B^{z^{*}}(x, y=\Delta y/2)\right\rangle\end{aligned} \tag{3.13b}$$

Here again, $B^{z^{**}}(x=\Delta x/2, y=\Delta y/2)$ and $B^{z^{**}}(x=-\Delta x/2, y=\Delta y/2)$ are magnetic induction components that are obtained at the endpoints of the upper y-face. They are obtained by the application of a two-dimensional Riemann solver at the edges of the mesh (explicit expressions are given below). One-dimensional Riemann problems in the upper face being considered will furnish the $B^{z^{*}}(x, y=\Delta y/2)$ component of the magnetic induction field that is to be used in the angled brackets:

$$\left\langle B^{z^{*}}(x, y=\Delta y/2)\right\rangle = \frac{1}{\Delta x}\int_{-\Delta x/2}^{+\Delta x/2} B^{z^{*}}(x, y=\Delta y/2)\,dx.$$

These Riemann problems are solved at each of the quadrature points in the y-face. Let the two states have subscripts D (for down) and U (for upper). Then $B^{z^{*}}(x, y=\Delta y/2)$ is given explicitly by

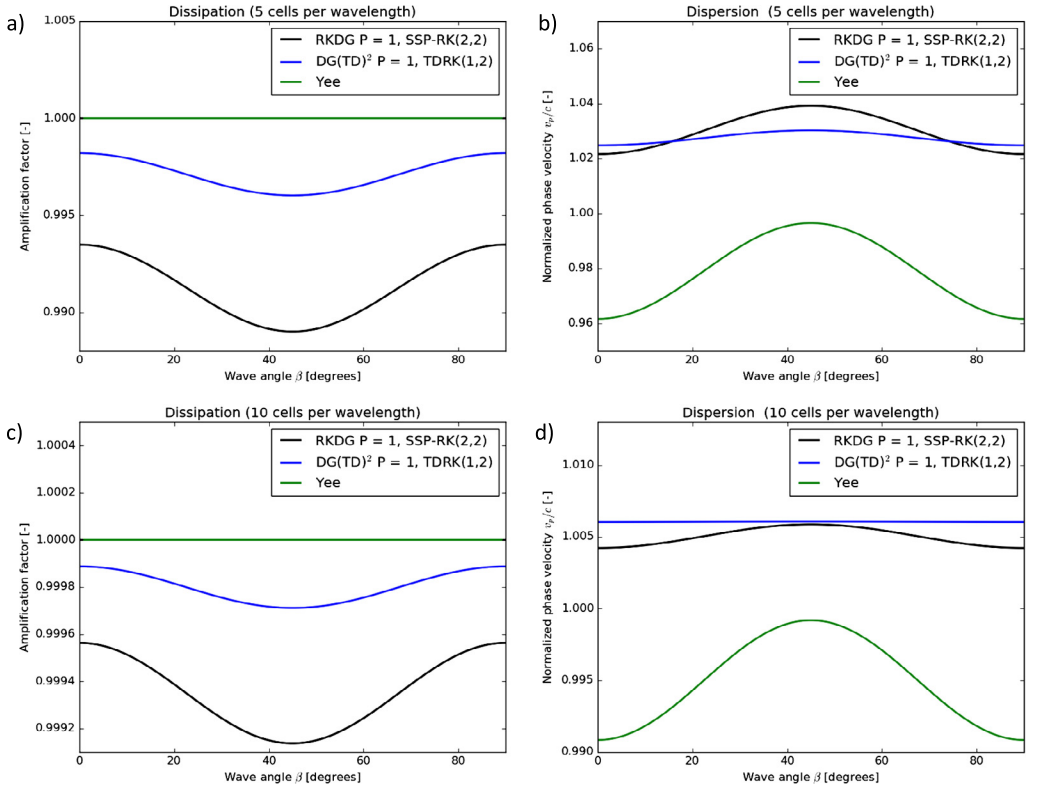

Fig. 2. For the second order DG(TD)2 scheme, we plot out the dissipation and dispersion for electromagnetic waves that span five and ten zones. For comparison purposes, we also show the same information for second order DGTD with SSP-RK timestepping and second order FDTD schemes. Figs. 2a and 2b show the dissipation and dispersion for waves that span five zones and propagate at all possible directions on a Cartesian mesh. Figs. 2c and 2d show the dissipation and dispersion for waves that span ten zones and propagate at all possible directions on a Cartesian mesh.

$$B^{z^*} = \frac{1}{2}\left(B^z_D + B^z_U\right) + \frac{1}{2c}\left(D^y_U/\varepsilon - D^y_D/\varepsilon\right). \tag{3.14}$$

The two-dimensional Riemann solver will provide the magnetic induction $B^{z^{**}}\,(x = \pm\Delta x/2,\, y = \pm\Delta y/2)$ at the edges of the mesh. Let the four states that come together be labeled by subscripts RU (for right-upper), LU (for left-upper), LD (for left-down) and RD (for right-down). Then $B^{z^{**}}\,(x = \Delta x/2,\, y = \Delta y/2)$ is given explicitly by

$$\begin{aligned} B^{z^{**}} = {} & \frac{1}{4}\left(B^z_{LD} + B^z_{LU} + B^z_{RD} + B^z_{RU}\right) \\ & + \frac{1}{2c}\left(\frac{1}{2}\left(D^x_{LU}/\varepsilon + D^x_{RU}/\varepsilon\right) - \frac{1}{2}\left(D^x_{LD}/\varepsilon + D^x_{RD}/\varepsilon\right)\right). \\ & - \frac{1}{2c}\left(\frac{1}{2}\left(D^y_{RD}/\varepsilon + D^y_{RU}/\varepsilon\right) - \frac{1}{2}\left(D^y_{LD}/\varepsilon + D^y_{LU}/\varepsilon\right)\right) \end{aligned} \tag{3.15}$$

We refer to Balsara et al. [15], [16] for complete derivation and further details.

Eqs. (3.11a) and (3.13a) taken together also ensure that the mean electric displacement field components within the faces of the mesh preserve the constraint-preserving property at a discrete level. In other words, we retrieve the traditional Yee-type update.

The evolution equations for the modes of the z-component of the magnetic induction are obtained by instantiating Eq. (3.7) at a z-face. Note that suppressing the z-variation implies that both the near and far z-faces of Fig. 1 have the same z-component of the magnetic induction vector, thus ensuring that the solenoidality constraint in Eq. (3.3) is always satisfied for the magnetic induction. (The far z-face in Fig. 1 is not shown.) With $\hat{\mathbf{n}} = \hat{\mathbf{z}}$ and the test function $\phi\,(x, y) = 1$ in Eq. (3.7) then gives us

$$\begin{aligned} \frac{dB^z_0\,(t)}{dt} = {} & -\frac{1}{\varepsilon}\frac{1}{\Delta x}\left[\left\langle D^{y^*}\,(x = \Delta x/2,\, y)\right\rangle - \left\langle D^{y^*}\,(x = -\Delta x/2,\, y)\right\rangle\right] \\ & + \frac{1}{\varepsilon}\frac{1}{\Delta y}\left[\left\langle D^{x^*}\,(x,\, y = \Delta y/2)\right\rangle - \left\langle D^{x^*}\,(x,\, y = -\Delta y/2)\right\rangle\right] \end{aligned} \tag{3.16a}$$

Alike, with $\hat{\mathbf{n}} = \hat{\mathbf{z}}$ and the test function $\phi(x, y) = (x/\Delta x)$ in Eq. (3.7) also gives us

$$\begin{aligned}\frac{dB_x^z(t)}{dt} = &-\frac{1}{\varepsilon}\frac{6}{\Delta x}\left[\left\langle D^{y^*}(x = \Delta x/2, y)\right\rangle + \left\langle D^{y^*}(x = -\Delta x/2, y)\right\rangle\right] \\ &+ \frac{1}{\varepsilon}\frac{12}{\Delta y}\left[\left\langle (x/\Delta x)\, D^{x^*}(x, y = \Delta y/2)\right\rangle - \left\langle (x/\Delta x)\, D^{x^*}(x, y = -\Delta y/2)\right\rangle\right] + \frac{1}{\varepsilon}\frac{12}{\Delta x}\left\{D^y(x, y)\right\}\end{aligned} \tag{3.16b}$$

And finally, with $\hat{\mathbf{n}} = \hat{\mathbf{z}}$ and the test function $\phi(x, y) = (y/\Delta y)$ in Eq. (3.7) further gives us

$$\begin{aligned}\frac{dB_y^z(t)}{dt} = &-\frac{1}{\varepsilon}\frac{12}{\Delta x}\left[\left\langle (y/\Delta y)\, D^{y^*}(x = \Delta x/2, y)\right\rangle - \left\langle (y/\Delta y)\, D^{y^*}(x = -\Delta x/2, y)\right\rangle\right] \\ &+ \frac{1}{\varepsilon}\frac{6}{\Delta y}\left[\left\langle D^{x^*}(x, y = \Delta y/2)\right\rangle + \left\langle D^{x^*}(x, y = -\Delta y/2)\right\rangle\right] - \frac{1}{\varepsilon}\frac{12}{\Delta y}\left\{D^x(x, y)\right\}\end{aligned} \tag{3.16c}$$

From the above three equations, note that angled brackets again represent suitably high order line averages in the edges that surround the z-face. Notice that the angled brackets in the above three equations contain the electric displacements obtained from one-dimensional Riemann solvers. In x-direction we have two states, labeled by L (for left) and R (for right), coming together. The solution of the one-dimensional Riemann problem is then given explicitly by

$$D^{y^*} = \frac{1}{2}\left(D_L^y + D_R^y\right) - \frac{c\varepsilon}{2}\left(B_R^z - B_L^z\right). \tag{3.17}$$

Likewise, in y-direction we have two states, labeled by D (for down) and U (for upper), coming together. The solution of the resulting one-dimensional Riemann problem is

$$D^{x^*} = \frac{1}{2}\left(D_D^x + D_U^x\right) + \frac{c\varepsilon}{2}\left(B_U^z - B_D^z\right). \tag{3.18}$$

Also notice the introduction of curly brackets, i.e. {}, in Eqs. (3.16b) and (3.16c). These curly brackets denote suitably high order area averages within the z-face of Fig. 1:

$$\left\{D^x(x, y)\right\} = \frac{1}{\Delta x \Delta y}\int_{-\Delta x/2}^{+\Delta x/2}\int_{-\Delta y/2}^{+\Delta y/2} D^x(x, y)\, dxdy.$$

As always, they have to be obtained via a suitably high order two-dimensional quadrature formula. Notice that in order to compute the angled brackets along the edges and the curly brackets over the faces, the electric displacement components D^x and D^y are needed at all locations in the zone. This is obtained by the constraint-preserving reconstruction developed in Section III of Balsara et al. [15].

Up to this point, the narrative in the previous three paragraphs, i.e. the narrative surrounding Eqs. (3.11), (3.13), (3.16), tracks the narrative in Balsara and Käppeli [18]. However, notice that in Balsara et al. [20] a new type of invention was made. It was based on a multidimensional GRP solver. The multidimensional GRP solver sits on top of the multidimensional Riemann solver. The multidimensional GRP solver takes in not just the input states of the multidimensional Riemann solver but also their spatial derivatives. For a *very small increase in computational complexity*, the multidimensional GRP solver returns not just the starred and double starred variables in Eqs. (3.11), (3.13), (3.16) but also their time-derivatives. As a result, if we think of Eqs. (3.11), (3.13), (3.16) as being analogous to Eq. (2.1) then we realize that the right-hand sides of those equations give us the analogue of $\mathbf{F}(\mathbf{U})$. Now realize that the multidimensional GRP solver gives us the time-derivative of the right-hand sides of Eqs. (3.11), (3.13), (3.16); i.e. the analogue of $\dot{\mathbf{F}}(\mathbf{U})$. As a result, a second order accurate in space and time scheme can be devised by the following time-stepping strategy

$$\mathbf{U}^{n+1} = \mathbf{U}^n + \Delta t \mathbf{F}\left(\mathbf{U}^n\right) + \frac{\Delta t^2}{2}\dot{\mathbf{F}}\left(\mathbf{U}^n\right) \tag{3.19}$$

The point to be emphasized is that this is all achieved with a very small increase in computational cost. But there is a catch which is easy to miss. The update must be *truly multidimensional*, in keeping with the fact that the governing PDE is also truly multidimensional.

For the sake of completeness, we now give explicit expressions for the time-derivatives obtained from the multidimensional GRP solver. We specialize the expressions for the here considered simplified CED equations. For a complete derivation and full generality, we refer to Balsara et al. [20]. Let us begin with the time-derivatives of the right-hand sides of Eqs. (3.11) and (3.13). For the right x-face at $x = +\Delta x/2$ with a left (L) and right (R) state interacting, the time-derivative of the magnetic induction $\dot{B}^{z^*}(x = \Delta x/2, y)$ is given explicitly by

$$\begin{aligned}\dot{B}^{z^*} = &-\left[\frac{1}{2\varepsilon}\left(\left(\frac{\partial D^y}{\partial x}\right)_L + \left(\frac{\partial D^y}{\partial x}\right)_R\right) - \frac{c}{2}\left(\left(\frac{\partial B^z}{\partial x}\right)_R - \left(\frac{\partial B^z}{\partial x}\right)_L\right)\right] \\ &+\left[\frac{1}{2\varepsilon}\left(\left(\frac{\partial D^x}{\partial y}\right)_L + \left(\frac{\partial D^x}{\partial y}\right)_R\right)\right]\end{aligned} \tag{3.20}$$

For the upper y-face at $y = +\Delta y/2$ with a down (D) and upper (U) state interacting, the time-derivative of the magnetic induction $\dot{B}^{z^*}(x, y = \Delta y)$ is given explicitly by

$$\begin{aligned}\dot{B}^{z^*} = &-\left[\frac{1}{2\varepsilon}\left(\left(\frac{\partial D^y}{\partial x}\right)_D + \left(\frac{\partial D^y}{\partial x}\right)_U\right)\right] \\ &+\left[\frac{1}{2\varepsilon}\left(\left(\frac{\partial D^x}{\partial y}\right)_D + \left(\frac{\partial D^x}{\partial y}\right)_U\right) + \frac{c}{2}\left(\left(\frac{\partial B^z}{\partial y}\right)_U - \left(\frac{\partial B^z}{\partial y}\right)_D\right)\right]\end{aligned} \tag{3.21}$$

Eqs. (3.20) and (3.21) are the time-derivatives of Eqs. (3.12) and (3.14), respectively. For the time-derivative of the magnetic induction along the edges of the mesh with right-upper (RU), left-upper (LU), left-down (LD) and right-down (RD) states interacting, the time-derivative $\dot{B}^{z^{**}}(x = \pm\Delta x/2, y = \pm\Delta y/2)$ is explicitly given by

$$\begin{aligned}\dot{B}^{z^{**}} = &-\frac{1}{4\varepsilon}\left(\left(\frac{\partial D^y}{\partial x}\right)_{LD} + \left(\frac{\partial D^y}{\partial x}\right)_{LU} + \left(\frac{\partial D^y}{\partial x}\right)_{RD} + \left(\frac{\partial D^y}{\partial x}\right)_{RU}\right) \\ &+\frac{c}{4}\left(\left(\frac{\partial B^z}{\partial x}\right)_{RD} + \left(\frac{\partial B^z}{\partial x}\right)_{RU} - \left(\frac{\partial B^z}{\partial x}\right)_{LD} - \left(\frac{\partial B^z}{\partial x}\right)_{LU}\right) \\ &+\frac{1}{4\varepsilon}\left(\left(\frac{\partial D^x}{\partial x}\right)_{RU} - \left(\frac{\partial D^x}{\partial x}\right)_{RD} - \left(\frac{\partial D^x}{\partial x}\right)_{LU} + \left(\frac{\partial D^x}{\partial x}\right)_{LD}\right) \\ &+\frac{1}{4\varepsilon}\left(\left(\frac{\partial D^x}{\partial y}\right)_{LD} + \left(\frac{\partial D^x}{\partial y}\right)_{LU} + \left(\frac{\partial D^x}{\partial y}\right)_{RD} + \left(\frac{\partial D^x}{\partial y}\right)_{RU}\right) \\ &+\frac{c}{4}\left(\left(\frac{\partial B^z}{\partial y}\right)_{LU} + \left(\frac{\partial B^z}{\partial y}\right)_{RU} - \left(\frac{\partial B^z}{\partial y}\right)_{LD} - \left(\frac{\partial B^z}{\partial y}\right)_{RD}\right) \\ &-\frac{1}{4\varepsilon}\left(\left(\frac{\partial D^y}{\partial y}\right)_{RU} - \left(\frac{\partial D^y}{\partial y}\right)_{LU} - \left(\frac{\partial D^y}{\partial y}\right)_{RD} + \left(\frac{\partial D^y}{\partial y}\right)_{LD}\right)\end{aligned} \tag{3.22}$$

Eqn. (3.22) is the time-derivative of Eq. (3.15). Next let us focus on the time-derivatives of the right-hand sides of Eqs. (3.16). For the right x-face at $x = +\Delta x/2$ with a left (L) and right (R) state interacting, the time-derivative of the electric displacement $\dot{D}^{y^*}(x = \Delta x/2, y)$ is given explicitly by

$$\dot{D}^{y^*} = -\frac{c^2\varepsilon}{2}\left(\left(\frac{\partial B^z}{\partial x}\right)_L + \left(\frac{\partial B^z}{\partial x}\right)_R\right) + \frac{c}{2}\left(\left(\frac{\partial D^y}{\partial x}\right)_R - \left(\frac{\partial D^y}{\partial x}\right)_L\right) \tag{3.23}$$

For the upper y-face at $y = +\Delta y/2$ with a down (D) and upper (U) state interacting, the time-derivative of the electric displacement $\dot{D}^{x^*}(x, y = \Delta x/2)$ is given explicitly by

$$\dot{D}^{x^*} = +\frac{c^2\varepsilon}{2}\left(\left(\frac{\partial B^z}{\partial y}\right)_D + \left(\frac{\partial B^z}{\partial y}\right)_U\right) + \frac{c}{2}\left(\left(\frac{\partial D^x}{\partial y}\right)_U - \left(\frac{\partial D^x}{\partial y}\right)_D\right) \tag{3.24}$$

Eqs. (3.23) and (3.24) are the time-derivatives of Eqs. (3.17) and (3.18), respectively. Note that the spatial derivatives in the above expressions are readily obtained from the modes evolved in the DG(TD)^2 schemes.

Let us emphasize the last point from the previous two paragraphs in considerable detail; just to make sure that the message is driven home. In Eqs. (3.11), (3.13), (3.16), the double starred variables on the right-hand sides will indeed get multidimensional updates because they are obtained from a multidimensional GRP solver. That solver will indeed factor in all the spatial derivatives and include them in the update using a Cauchy-Kovalevskaya procedure. However, notice that Eqs. (3.11b) and (3.13b) also involve single starred variables. If one is using a DGTD update of the sort that is described in Balsara and Käppeli [18] then it is indeed acceptable to use a one-dimensional Riemann solver for the update of the angled brackets in Eqs. (3.11b) and (3.13b). *However*, if one is using a DG(TD)^2 update of the sort described here, then the time-derivatives of the single starred variables in those angled brackets *must* include the gradients in the directions that are transverse to the direction of the GRP in addition to including the gradients that are in the direction of the GRP! A similar consideration applies to the single starred variables within the angled brackets in Eqs. (3.16). *Furthermore*, consider the terms within the curly brackets in Eqs. (3.16b) and (3.16c); the terms within those curly brackets *must* also be updated multidimensionally. It is only when all the potential multidimensional effects are included that the resulting DG(TD)^2 scheme becomes stable and consistent with the governing PDE.

In this Sub-section we have shown how to start with a globally constraint-preserving DGTD scheme for CED and upgrade it to yield a globally constraint-preserving DG(TD)^2 scheme for CED. In this Sub-section, we have carried out such an exercise

in great detail for the second order DGTD scheme in Balsara and Käppeli [18]. We now point out that Section 4 of Balsara and Käppeli [18] also describes a globally constraint-preserving third order DGTD scheme and Appendix B of the same paper describes an analogous fourth order DGTD scheme. As a result, it is now possible to upgrade those DGTD schemes to yield higher order globally constraint-preserving DG(TD)^2 schemes for CED.

3.2. von Neumann stability of the second order, single-stage DG(TD)^2 scheme

Eqn. (3.19) from the previous Sub-section can be combined with the analysis in Sub-section 3.2 from Balsara and Käppeli [18]. This gives us a strategy for carrying out a von Neumann stability analysis of the second order, single-stage DG(TD)^2 scheme described in the previous Sub-section. The scheme has a maximal CFL number of 0.25. The same CFL was obtained in Balsara and Käppeli [18] where second order SSP-RK timestepping was conjoined with DG schemes for CED. We see, therefore, that the CFL stemming from the use of TDRK timestepping is the same as the CFL stemming from the use of SSP-RK timestepping.

In CED we would like electromagnetic waves to propagate as isotropically as possible relative to the computational mesh. They should propagate with speeds that are as close as possible to the speed of light. Since electromagnetic waves are not dissipated as they propagate in perfect insulators with uniform dielectric properties, we want the dissipation of the numerical scheme to be as small as possible. Moreover, we would like all these desirable properties to hold for electromagnetic waves with a wavelength that spans as few zones as possible. We are helped in this regard by the fact that our DG(TD)^2 scheme is linear, at least when limiters are not used. The von Neumann stability analysis can give us an abundance of insights with regard to electromagnetic wave propagation on a Cartesian computational mesh. Operationally, we work on a Cartesian mesh with $\Delta x = \Delta y$. Fig. 4.2 from Taflove and Hagness [57] presents a von Neumann analysis-based study of electromagnetic wave propagation in FDTD, thereby providing the motivation for an analogous study in this section. We now ask the important question: Does the resulting scheme give us any advantage in terms of dissipation or dispersion?

For the results shown in this Sub-section, we held the CFL number to be 95% of the maximal allowable CFL number. For each direction of electromagnetic wave propagation, the von Neumann stability analysis then gives us an amplification factor which is the largest absolute value of the eigenvalues of the amplification matrix. It also gives us a phase speed for the propagation of the waves. Ideally, we want the amplification factor to be as close to unity as possible. We also want the phase speed of the waves to be as close to the speed of light as possible. For the second order DG(TD)^2 scheme, we plot out the dissipation and dispersion for electromagnetic waves that span five and ten zones. For comparison purposes, we also show the same information for second order DGTD with SSP-RK timestepping and second order FDTD schemes. Figs. 2a and 2b show the dissipation and dispersion for waves that span five zones and propagate at all possible directions on a Cartesian mesh. Figs. 2c and 2d show the dissipation and dispersion for waves that span ten zones and propagate at all possible directions on a Cartesian mesh. We see that the Yee scheme is dissipation-free, as expected for a scheme that uses a symplectic (leap frog) time update strategy. But we also happily notice from Figs. 2a and 2c that the second order DG(TD)^2 scheme has lower dissipation compared to second order DGTD scheme from Balsara and Käppeli [18] that utilizes SSP-RK timestepping. We attribute that to the fact that the time update for the second order DG(TD)^2 scheme in Eq. (3.19) is better centered in time. Now let us compare Figs. 2b and 2d for the dispersion properties of the schemes that we are considering. We clearly see that all second order DG schemes offer better dispersion properties compared to the second order FDTD scheme. Furthermore, we find that the second order DG(TD)^2 scheme offers more isotropic propagation of electromagnetic radiation compared to the second order DGTD scheme from Balsara and Käppeli [18] that utilizes SSP-RK timestepping. This shows us that DG(TD)^2 schemes have some desirable properties which could even be improved on as we go to higher orders. The narrative in this Sub-section has, therefore, given us incentive to develop DG(TD)^2 schemes with even higher orders of accuracy.

4. Optimal DG(TD)^2 schemes at third order

In this section we demonstrate how the two-stage TDRK timestepping scheme from Sub-section 2.1 can be optimized to yield a third order, two-stage DG(TD)^2 scheme for CED. In this paper we show how the resulting scheme can be optimized to have some desirable features. These schemes derive their value from the fact that much of the information that is used in the construction of a Riemann solver can indeed be re-used in the construction of the GRP solver. As a result, one gets the GRP solver for only a mild amount of additional cost compared to a Riemann solver. But the payoff, in terms of improved CFL, lower dissipation and lower dispersion can be substantial.

This section has been split into two sub-sections. Sub-section 4.1 describes the optimization of the third order, two-stage DG(TD)^2 scheme. Sub-section 4.2 describes the results from the von Neumann stability analysis of the third order, two-stage DG(TD)^2 scheme.

4.1. Optimization of the third order, two-stage DG(TD)^2 scheme

We would, of course, like to maximize the CFL. But we would also like to maximize the CFL within the context of obtaining a scheme that has low dissipation and low dispersion. This identifies the desirable features that we would pick out, though to some extent the choice is subjective. In Sub-section 2.1 we identified a two-parameter (u_1, u_2) space. For each

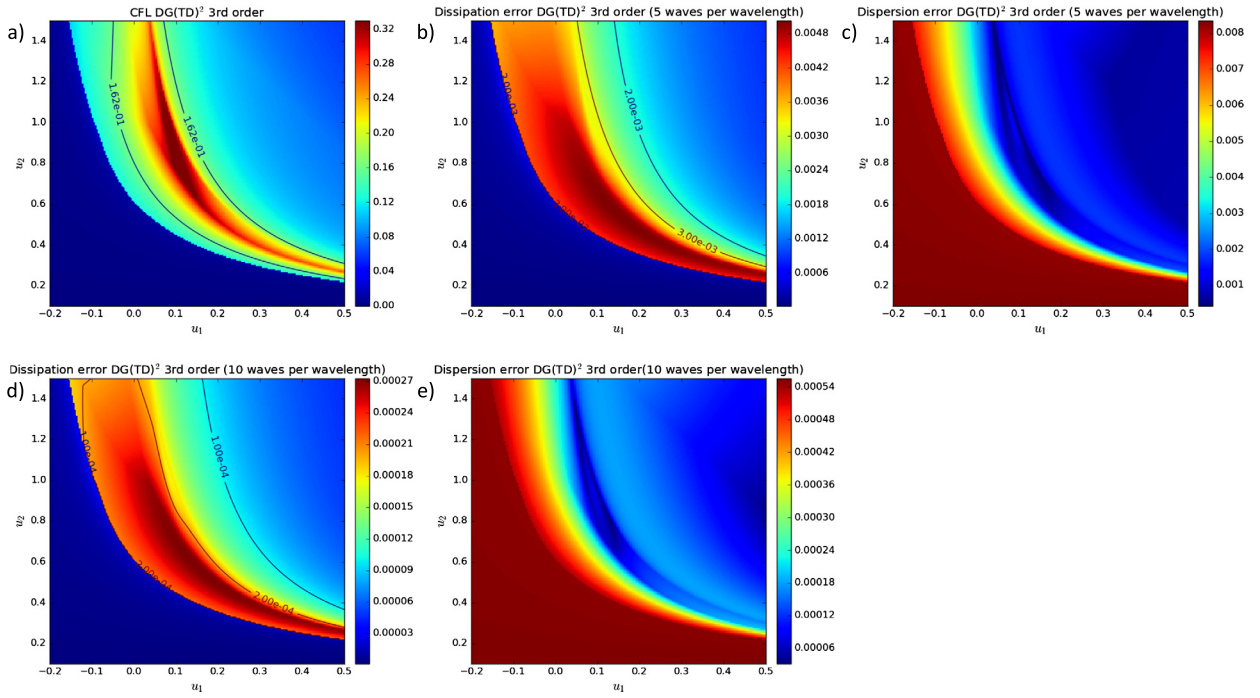

Fig. 3. Fig. 3a shows the permitted CFL in the two-parameter space. Figs. 3b and 3c show us the maximum dissipation and dispersion error that an electromagnetic wave spanning five zones would have if it were propagated at any angle on a Cartesian mesh. Figs. 3d and 3e show us the maximum dissipation and dispersion error that an electromagnetic wave spanning ten zones would have if it were propagated at any angle on a Cartesian mesh.

point in this space we can evaluate one or the other desirable feature. Fig. 3a shows the permitted CFL in the two-parameter space. Figs. 3b and 3c show us the maximum dissipation and dispersion errors that an electromagnetic wave spanning five zones would have if it were propagated at any angle on a Cartesian mesh. Figs. 3d and 3e show us the maximum dissipation and dispersion errors that an electromagnetic wave spanning ten zones would have if it were propagated at any angle on a Cartesian mesh. Such plots can be obtained from a von Neumann stability analysis of the DG scheme. For our purposes, the lowest possible dissipation corresponds to an amplification factor of unity, as obtained from the von Neumann stability analysis. Consequently, Figs. 3b and 3d plot out the maximum of the absolute value of the deviation of the amplification factor from unity. Furthermore, for our purposes, the lowest possible dispersion corresponds to a phase of propagation that coincides with the speed of light. For the phase error we evaluate the fractional deviation of the numerical phase speed $\tilde{v}_p$ from the speed of light c (i.e., we consider $(\tilde{v}_p - c)/c$). These deviations can again be obtained from the von Neumann stability analysis. Consequently, Figs. 3c and 3e plot out the maximum of the absolute value of the deviation in the fractional phase speed from zero. In other words, optimal wave propagation with the true speed of light would cause the deviation in the phase speed to become zero.

Fig. 3a shows us the region of parameter space where the CFL is colorized for each point in parameter space. The sub-regions of parameter space where the CFL is close to maximum is shown by a deep red color in Fig. 3a. However, let us also focus on Figs. 3b and 3c which colorize the dissipation and dispersion errors. Since the dissipation is the more important parameter, we overplot on Fig. 3b the contours that correspond to a maximum deviation of the amplification factor from unity by two parts in a thousand and three parts in a thousand. Since the waves in Figs. 3d and 3e span ten zones, we overplot on Fig. 3d the contours that correspond to a maximum deviation of the amplification factor from unity by one part in ten-thousand and three parts in ten-thousand. We see that, generally speaking, the dissipation becomes smaller as we move in a north-easterly direction in Figs. 3b and 3d. Likewise, the phase accuracy improves as we move in a north-easterly direction in Figs. 3c and 3e. Now let us circle back to Fig. 3a. We realize that the ranges of parameters that would give us exceptionally low dissipation and exceptionally low dispersion would also force us to settle for an exceptionally low CFL. This is why we have to optimize our choices. We do that next.

We see from Fig. 3a that we could get a CFL that is as large as 0.34. However, from Figs. 3b and 3d we see that such a scheme would have substantial dissipation. Similarly, we see from Figs. 3c and 3e that the scheme would have substantial dispersion. We therefore ask, “What is the acceptable range of CFLs that we could tolerate, and furthermore, where in the two-parameter plot of Fig. 3a are those CFLs reached?”. The two solid curves in Fig. 3a correspond to a CFL of 0.162, which was the largest CFL that Balsara and Käppeli [18] found for three-stage, SSP-RK-based, DGTD schemes for CED. To show some advantage in our new two-stage DG(TD)^2 scheme, we would like it to match or improve on the CFL of the SSP-RK-based, DGTD scheme (recall that the latter scheme had a limiting CFL of 0.162). That is why we overplotted the solid lines in Fig. 3a. The colors in Fig. 3a prevent us from seeing the overplotted lines very clearly, which is why we present Fig. 4. In

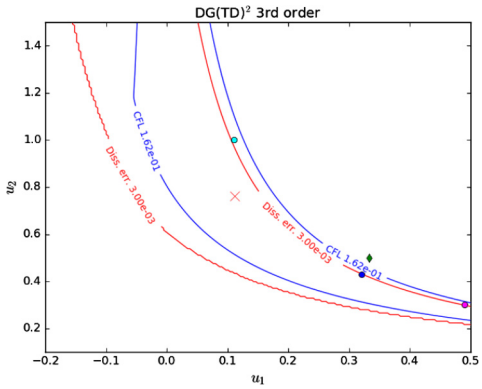

Fig. 4. In Fig. 4 we remove the colorization from Fig. 3a, we retain the blue solid lines from Fig. 3a and we also overlay, as two red curves, the lower contour from Fig. 3b. Apart from that, Fig. 4 shows the same two-parameter space as Fig. 3a. The magenta, blue and green circles that are shown in Fig. 4 identify a reasonable search space where we will look for optimal schemes with the aid of the human eye and human intuition. The green diamond shows the location of the fourth order scheme. The red cross shows the location of the scheme that produces the largest CFL.

Fig. 4 we remove the colorization from Fig. 3a, we retain the blue solid lines from Fig. 3a and we also overlay, as red curves, the lower contour from Fig. 3b. Apart from that, Fig. 4 shows the same two-parameter space as Fig. 3a. (The lower contour in Fig. 3d is not as restrictive as the lower contour in Fig. 3b, which is why we show only the lower contour from Fig. 3b.) An optimal scheme should lie north-east of that lower contour in Fig. 4 and it should also retain a robust CFL. We, therefore, see that the range of parameters where we would get optimal schemes is indeed very limited – but it is not a null set! The logic of this paragraph and the previous paragraph illustrates that an optimal region can be found and that it can be found simply by asking a computer to span a very large parameter space. I.e. the machine teaches us where to look for optimal schemes. The magenta, blue and green circles that are shown in Fig. 4 identify a reasonable search space where we will look for optimal schemes with the aid of the human eye and human intuition. The green diamond shows the location of the fourth order scheme. Clearly, we see that the fourth order scheme will have too small a CFL; i.e. a CFL of 0.1323 which is less than 0.162. The red cross shows the location in parameter space of the scheme that produces the largest CFL of 0.34.

4.2. von Neumann stability of the third order, two-stage DG(TD)^2 scheme

The next step in the optimization process requires combining human intuition and an optimization algorithm.

First let us start with human intuition. For each of the circles that we identified in Fig. 4, we plot out the dissipation and dispersion for electromagnetic waves that span five and ten zones. Figs. 5a and 5b show the dissipation and dispersion for waves that span five zones and propagate at all possible directions on a Cartesian mesh. Figs. 5c and 5d show the dissipation and dispersion for waves that span ten zones and propagate at all possible directions on a Cartesian mesh. The black curves in Fig. 5 show the third order, three-stage SSP-RK-based, DGTD scheme from Balsara and Käppeli [18]. The green curves in Fig. 5 show the use of a fourth order TDRK timestepping from Eq. (2.8); this scheme has a smaller CFL of 0.1323 and is third order accurate in space while retaining fourth order accuracy in time. It corresponds to parameters that are shown by the green diamond in Fig. 4. We see that it is an improvement over the third order DGTD scheme from Balsara and Käppeli [18]; but it suffers from a smaller CFL. The aquamarine, magenta and blue curves in Fig. 5 correspond to the parameters shown with the aquamarine, magenta and blue circles in Fig. 4. The red curves in Fig. 5 show the scheme that has the optimal CFL of 0.34 and corresponds to the red cross in Fig. 4.

We can now begin to understand the different schemes that we have generated using our human intuition. Let us first focus on the red curves in Fig. 5. These curves correspond to the two-stage, third-order DG(TD)^2 scheme that has the largest possible CFL. While we would be inclined to like this scheme based on the machine search, Figs. 5a and 5c show us that the scheme only achieves its large CFL at the expense of introducing substantial dissipation. Furthermore, we see that waves that are propagating in mesh-aligned directions will also suffer from dissipation. We would like to have a scheme that shows minimal dissipation for wave propagation in mesh-aligned directions. For this reason, we use our human intuition to realize that despite the optimal CFL, this scheme is not the most attractive scheme. We also see that the green curve in Fig. 5 produces the least overall dissipation. Therefore, if one is willing to tolerate a lower CFL, the third order in space DG(TD)^2 scheme that uses the fourth order TDRK timestepping from Eq. (2.8) would also be acceptable. Focus now on the aquamarine, magenta and blue curves in Figs. 5b and 5d. We see that they have dispersion properties that are slightly superior to both the green curve and the black curve. Their CFL is also substantially larger than 0.1323 or 0.162, indicating a clear advantage. Now focus on the aquamarine, magenta and blue curves in Figs. 5a and 5c. We see that they have substantially lower dissipation compared to the black curve (which is the original third order DGTD scheme from Balsara and Käppeli [18])! Clearly, the SSP-RK is a sub-optimal timestepping strategy for CED. We see, however, that the aquamarine, magenta and blue curves have dissipation that is slightly inferior to the dissipation in the green curve, as expected. We see, therefore, that our optimization exercise has produced several positive results.

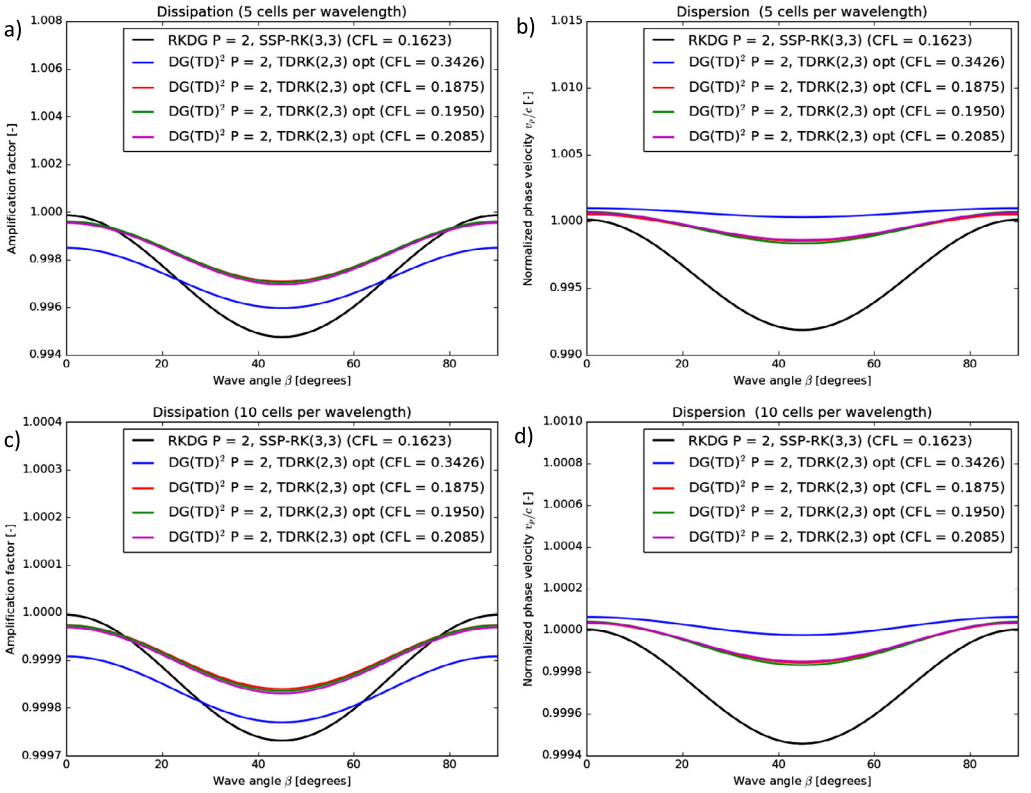

Fig. 5. For each of the dots that we identified in Fig. 4, we plot out the dissipation and dispersion for electromagnetic waves that span five and ten zones. The human-optimized schemes are shown. Figs. 5a and 5b show the dissipation and dispersion for waves that span five zones and propagate at all possible directions on a Cartesian mesh. Figs. 5c and 5d show the dissipation and dispersion for waves that span ten zones and propagate at all possible directions on a Cartesian mesh. The original third order DGTD scheme with SSP-RK timestepping is also shown to provide a point of reference.

The blue dot in Fig. 4 is especially noteworthy because it identifies the parameters that are closest to the green diamond in Fig. 4. This also gives us the realization that scheme performance is smoothly varying in many parts of the search space (though not in all parts of the search space). Therefore, we get the idea that we can use one optimal scheme to discover other contiguous schemes that are optimized to have slightly different advantages. For these reasons we accept the blue dot in Fig. 4 as providing us with the optimal scheme. It has $(u_1, u_2) = (0.32, 0.43)$. With this choice of optimized parameters we can finally write down the optimal, third order DG(TD)^2 scheme by specifying the coefficients in Eq. (2.3) as:

$$a_{21} = \frac{43}{100}; \quad \hat{a}_{21} = \frac{1849}{2000}; \quad b_1 = \frac{3803}{5547}; \quad b_2 = \frac{1744}{5547}; \\ \hat{b}_1 = \frac{289}{6450}; \quad \hat{b}_2 = \frac{8}{25} \tag{4.1}$$

This completes our description of the optimized third order DG(TD)^2 scheme for CED that was obtained from human intuition. It has a CFL of 0.2085.

We now realize that relying on human intuition is a slow and sub-optimal process. Therefore, we ask a computer to use the optimization algorithms in Powell [45], [46] and Johnson [41] to optimize further. Many promising DG(TD)^2 schemes were found, including one which had dissipation and dispersion that were lower than the one in Eq. (4.1) along with offering a larger CFL of 0.2571. We also obtained yet another scheme with a CFL of 0.3265, however, it again proved to have larger dissipation and dispersion than we would have liked. For the sake of completeness, Table 1 shows the full set of third order coefficients that we obtained along with their CFL. We encourage use of the last row of that table because it offers the best compromise between a reasonably large CFL along with very low dissipation and dispersion.

We now document the dissipation and dispersion properties of the optimal DG(TD)^2 scheme that we found through machine-driven optimization in Fig. 6. To give the reader perspective, we also show the analogous results from original the three-stage DGTD scheme from Balsara and Käppeli [18] which uses SSP-RK timestepping. We also show the results from the large CFL scheme that the machine found. We see that the dispersion and dissipation properties of the DGTD scheme from Balsara and Käppeli [18] are indeed somewhat inferior. The DG(TD)^2 scheme with a CFL of 0.2571 has dispersion that is comparable to the DG(TD)^2 scheme with a CFL of 0.3265. However, the former scheme has dissipation properties that are an improvement to the latter scheme, which is why we prefer the former scheme.

Table 1
Shows the full set of third order coefficients that we obtained along with their CFL. The first three rows document schemes that were obtained via human optimization. The last two rows document schemes that were obtained via machine optimization.

a_{21}	$\hat{a}_{21}$	b_1	b_2	$\hat{b}_1$	$\hat{b}_2$	CFL
$\frac{477}{625}$	$\frac{227529}{781250}$	$\frac{3925537}{5460696}$	$\frac{1535159}{5460696}$	$\frac{2494841}{14310000}$	$\frac{1111}{10000}$	0.3426
1	$\frac{1}{2}$	$\frac{76}{135}$	$\frac{59}{135}$	$-\frac{109}{900}$	$\frac{49}{100}$	0.1950
$\frac{43}{100}$	$\frac{1849}{20000}$	$\frac{3803}{5547}$	$\frac{1744}{5547}$	$\frac{289}{6450}$	$\frac{8}{25}$	0.2085
$\frac{5889}{10000}$	$\frac{34680321}{200000000}$	$\frac{61140707}{104040963}$	$\frac{42900256}{104040963}$	$\frac{2110609}{22083750}$	$\frac{101}{625}$	0.3265
$\frac{1057}{2000}$	$\frac{1117249}{8000000}$	$\frac{10857001}{16758735}$	$\frac{5901734}{16758735}$	$\frac{2904133}{31710000}$	$\frac{2223}{10000}$	0.2571

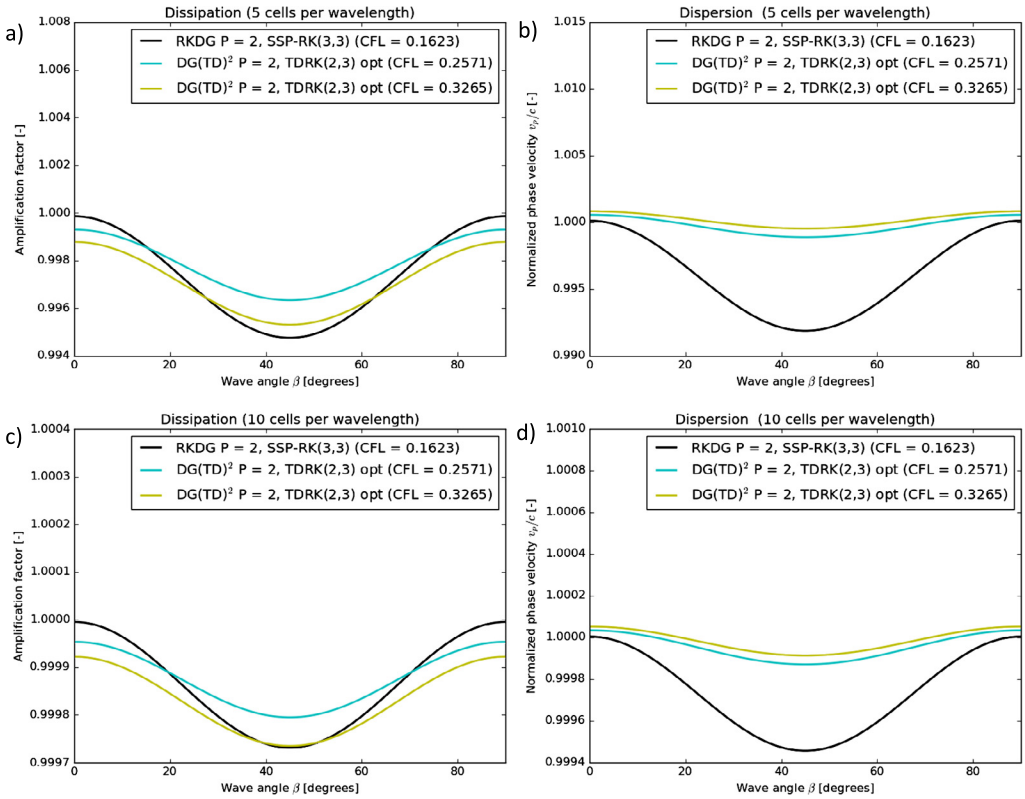

Fig. 6. Is identical in spirit to Fig. 5. However, it documents the dissipation and dispersion for electromagnetic waves that span five and ten zones for the machine-optimized third order schemes that we have found. The original third order DGTD scheme with SSP-RK timestepping is also shown to provide a point of reference.

Please notice that all but one of the schemes in Table 1 have positive coefficients. Only the second row in Table 1 has one negative coefficient; and that scheme was obtained by human optimization. In light of the fact that machine-driven optimization in Fig. 6 yields improved results to human-driven optimization, we now feel free to use machine-driven optimization in subsequent parts of the paper.

5. Optimal DG(TD)^2 schemes at fourth order

We now demonstrate how a three-stage TDRK timestepping scheme from Sub-section 2.2 can be optimized to yield a fourth order, three-stage DG(TD)^2 scheme for CED that has very desirable features. An examination of Eqs. (2.11) to (2.14) shows that we have eight equations and twelve free parameters in the TDRK time update. Therefore, it is a four parameter optimization and that is out of the scope of human-driven optimization. Consequently, we need to use machine-driven optimization using the software mentioned in the previous section. The objective is to maximize the CFL while fulfilling the eight order constraints. We will see that it indeed yields a scheme with minimal dissipation and dispersion. Fig. 7 is identical in spirit to Fig. 6. However, it documents the dissipation and dispersion for electromagnetic waves that span five and ten zones for the machine-optimized fourth order schemes that we have found. Our optimized DG(TD)^2 scheme allows a maximum CFL of 0.2322. The original fourth order DGTD scheme with SSP-RK timestepping is also shown in order

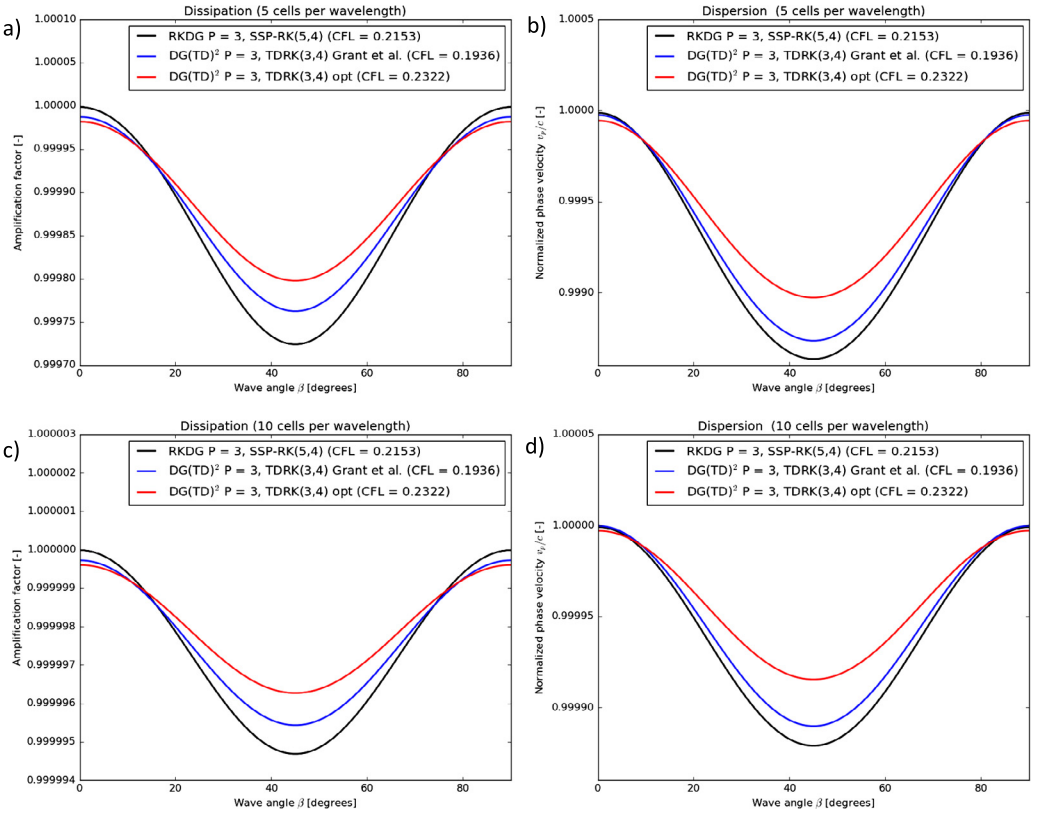

Fig. 7. Is identical in spirit to Fig. 6. However, it documents the dissipation and dispersion for electromagnetic waves that span five and ten zones for the machine-optimized fourth order schemes that we have found. The original fourth order DGTD scheme with SSP-RK timestepping is also shown to provide a point of reference.

to provide a point of reference; it allows a maximum CFL of 0.2153. We also show the SSP-TS scheme from Grant et al. [35]; which allows a maximum CFL of 0.1936. We see from Fig. 7 that the DG(TD)^2 scheme offers the lowest dissipation and dispersion amongst the three schemes that we have compared. The other two schemes in Fig. 7 have higher levels of dissipation, owing to the fact that they are SSP schemes. Comparing Fig. 7 to Fig. 6, we see that the optimized fourth order schemes are better compared to the optimized third order schemes.

Our task is now to document the fourth-order three-stage DG(TD)^2 schemes that we have found. Please refer to Eq. (2.10) for the coefficients. The optimal scheme, which minimizes dissipation and dispersion and permits a large CFL of 0.2322 is given by

$$
\begin{aligned}
&b_1 = 0.40947669189107749; && b_2 = 8.0434980657990901\text{E-}002; && b_3 = 0.51008832745093169;\\
&\hat{b}_1 = 5.4611648326405991\text{E-}002; && \hat{b}_2 = 2.7208570201466540\text{E-}003; && \hat{b}_3 = 5.6078083959227858\text{E-}002;\\
&a_{21} = 0.91883707684724236; && a_{31} = 0.49171927302523588; && a_{32} = 0.12127802834948631;\\
&\hat{a}_{21} = 0.42213078689459249; && \hat{a}_{31} = 6.8195421162713099\text{E-}002; && \hat{a}_{32} = 8.2526755291938963\text{E-}003;
\end{aligned}
\tag{5.1}
$$

For completeness, we also document the timestepping scheme from Grant et al. [35], which has a maximum CFL of 0.1936. Notice that because it is an SSP scheme, it has lower CFL and yet a larger amount of dissipation and dispersion. It is given by

$$
\begin{aligned}
&b_1 = \frac{17}{48}; \quad b_2 = \frac{1}{12}; \quad b_3 = \frac{27}{48};\\
&\hat{b}_1 = \frac{1}{24}; \quad \hat{b}_2 = 0; \quad \hat{b}_3 = 0\\
&a_{21} = 1; \quad a_{31} = \frac{14}{27}; \quad a_{32} = \frac{4}{27};\\
&\hat{a}_{21} = \frac{1}{2}; \quad \hat{a}_{31} = \frac{2}{27}; \quad \hat{a}_{32} = 0.
\end{aligned}
\tag{5.2}
$$

Table 2
Shows the accuracy analysis for the second-order DG(TD)^2 scheme for the propagation of an electromagnetic wave in vacuum. A CFL that was 95% of the maximum was used. The errors and accuracy in the y-component of the electric displacement vector (measured at the y-faces) and z-component of the magnetic induction (measured as zone averages) are shown.

Zones	D_y L_1 error	D_y L_1 accuracy	D_y L_{inf} error	D_y L_{inf} accuracy
8^2	1.74E-04	–	2.76E-04	–
16^2	3.64E-05	2.25	5.66E-05	2.29
32^2	8.21E-06	2.15	1.28E-05	2.14
64^2	1.98E-06	2.05	3.10E-06	2.05
128^2	4.88E-07	2.02	7.67E-07	2.02
256^2	1.22E-07	2.01	1.91E-07	2.01
512^2	3.03E-08	2.00	4.77E-08	2.00
Zones	B_z L_1 error	B_z L_1 accuracy	B_z L_{inf} error	B_z L_{inf} accuracy
8^2	9.24E-02	–	1.36E-01	–
16^2	1.89E-02	2.29	2.96E-02	2.20
32^2	4.32E-03	2.13	6.78E-03	2.13
64^2	1.05E-03	2.04	1.65E-03	2.04
128^2	2.60E-04	2.01	4.08E-04	2.01
256^2	6.47E-05	2.00	1.02E-04	2.00
512^2	1.62E-05	2.00	2.54E-05	2.00

It is also worth pointing out that the analysis of Grant et al. [35] was not based on having an underlying discretization of a PDE, whereas the analysis done here draws on a genuine PDE system. This completes our discussion of fourth-order three-stage DG(TD)^2 schemes.

6. Numerical tests

In this section, we present a numerical accuracy analysis of the second-, third- and fourth-order accurate DG(TD)^2 schemes designed in this paper. We use the same test setup as Balsara et al. [15]. The test problem consists of a plane polarized electromagnetic wave propagating in vacuum along the north-east diagonal of a uniformly discretized computational domain spanning $[-1/2, +1/2]^2$ meter with periodic boundary conditions. The magnetic induction is initialized with the following magnetic vector potential

$$\mathbf{A}(x, y, z, t) = \frac{1}{2\pi} \sin\left[2\pi\left(x + y - \sqrt{2}ct\right)\right] \hat{y}.$$

The components of the magnetic induction vector are then obtained at the zone faces by the well-known relationship $\nabla \times \mathbf{B}$. Likewise, the electric displacement is initialized with an electric vector potential given by

$$\mathbf{C}(x, y, z, t) = -\frac{1}{2\pi\sqrt{2}} \sin\left[2\pi\left(x + y - \sqrt{2}ct\right)\right] \hat{z}$$

and the components of the electric displacement vector are then obtained at the zone faces by the relation $\mathbf{D} = c\varepsilon_0(\nabla \times \mathbf{C})$. Here c is the speed of light and $\varepsilon_0 = 8.85 \times 10^{-12}$ F/m is the free space permittivity. The problem was run from initial time $t_0 = 0$ until $t_f = 1/\sqrt{2}c \approx 2.3587 \times 10^{-9}$ seconds when the wave has traveled once through the computational domain.

Tables 2, 3 and 4 show the accuracy analysis for the second-, third- and fourth-order DG(TD)^2 schemes. The errors and order of accuracy in the y-component of the electric displacement vector and the z-component of the magnetic induction are shown at final time t_f of the simulation. We observe that all the schemes indeed meet their design order of accuracy. As already observed for the RKDG schemes in Balsara and Käppeli [18], our novel DG(TD)^2 schemes have the very desirable property that they reach their design accuracies at fairly low resolutions.

In the considered idealized setting, Poynting's theorem implies that Maxwell's equations conserve the electromagnetic energy analytically. However, given the nature of our DG(TD)^2 schemes, energy conservation at the discrete level is not guaranteed. From the consistency of the schemes with Maxwell's equation, it is expected that the electromagnetic energy is conserved with near-perfect precision in the limit of high numerical resolution, i.e. when the electromagnetic waves are resolved by a large number of zones. Given the limitation in computational resources, it is therefore desirable that a scheme preserves the electromagnetic energy as well as possible on the smallest number of zones per wavelength.

In order to assess the energy conservation properties of the presented DG(TD)^2 schemes, we compute the electromagnetic energy after one periodic orbit as a function of the number of zones of the computational mesh for the second-, third- and fourth-order schemes. This is shown in Fig. 8. This figure should be compared to Fig. 9a in Balsara and Käppeli [18]. We observe that the new DG(TD)^2 schemes have considerably lower energy losses. For a more quantitative comparison, we also show the information in tabulated form in Table 5. The latter table has to be compared to the relevant entries (first

Table 3
Shows the accuracy analysis for the third-order DG(TD)^2 scheme for the propagation of an electromagnetic wave in vacuum. A CFL that was 95% of the maximum was used. The errors and accuracy in the y-component of the electric displacement vector (measured at the y-faces) and z-component of the magnetic induction (measured as zone averages) are shown.

Zones	D_y L_1 error	D_y L_1 accuracy	D_y L_{inf} error	D_y L_{inf} accuracy
8^2	6.28E-05	-	9.15E-05	-
16^2	7.26E-06	3.11	1.13E-05	3.02
32^2	8.77E-07	3.05	1.38E-06	3.04
64^2	1.08E-07	3.02	1.70E-07	3.02
128^2	1.35E-08	3.01	2.12E-08	3.01
256^2	1.68E-09	3.00	2.64E-09	3.00
512^2	2.10E-10	3.00	3.30E-10	3.00
Zones	B_z L_1 error	B_z L_1 accuracy	B_z L_{inf} error	B_z L_{inf} accuracy
8^2	3.01E-02	-	4.69E-02	-
16^2	3.69E-03	3.03	5.75E-03	3.03
32^2	4.57E-04	3.01	7.16E-04	3.01
64^2	5.70E-05	3.00	8.96E-05	3.00
128^2	7.14E-06	3.00	1.12E-05	3.00
256^2	8.93E-07	3.00	1.40E-06	3.00
512^2	1.12E-07	3.00	1.76E-07	3.00

Table 4
Shows the accuracy analysis for the fourth-order DG(TD)^2 scheme for the propagation of an electromagnetic wave in vacuum. A CFL that was 95% of the maximum was used. The errors and accuracy in the y-component of the electric displacement vector (measured at the y-faces) and z-component of the magnetic induction (measured as zone averages) are shown.

Zones	D_y L_1 error	D_y L_1 accuracy	D_y L_{inf} error	D_y L_{inf} accuracy
8^2	6.15E-06	–	9.56E-06	–
16^2	4.17E-07	3.88	6.54E-07	3.87
32^2	2.65E-08	3.98	4.15E-08	3.98
64^2	1.65E-09	4.00	2.60E-09	4.00
128^2	1.03E-10	4.00	1.62E-10	4.00
256^2	6.45E-12	4.00	1.01E-11	4.00
512^2	4.04E-13	4.00	6.35E-13	4.00
Zones	B_z L_1 error	B_z L_1 accuracy	B_z L_{inf} error	B_z L_{inf} accuracy
8^2	2.49E-03	–	3.71E-03	–
16^2	1.95E-04	3.67	3.03E-04	3.61
32^2	1.32E-05	3.88	2.07E-05	3.87
64^2	8.56E-07	3.95	1.34E-06	3.95
128^2	5.42E-08	3.98	8.51E-08	3.98
256^2	3.41E-09	3.99	5.36E-09	3.99
512^2	2.15E-10	3.99	3.37E-10	3.99

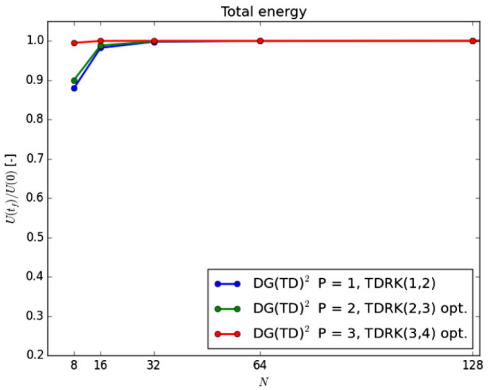

Fig. 8. Shows the electromagnetic energy after one periodic orbit as a function of number of zones along one direction of the two-dimensional mesh for second- (blue line), third- (green line) and fourth-order (red line) DG(TD)^2 schemes.

Table 5
Shows the quantitative values of the magnetic energy at the end of the simulation for the simulations documented in Fig. 8. We show the order of the scheme (and reconstruction strategy) and the kind of timestepping in the first two columns. The remaining columns show the resolution of the mesh and the electromagnetic energy in the simulation at the end of the run.

Scheme	Timestepping	8×8 zones	16×16 zones	32×32 zones	64×64 zones	128×128 zones
DG P = 1	TDRK(1, 2)	0.880	0.982	0.998	1.000	1.000
DG P = 2	TDRK(2, 3) opt.	0.900	0.988	0.999	1.000	1.000
DG P = 3	TDRK(3, 4) opt.	0.995	1.000	1.000	1.000	1.000

Table 6
Shows the runtime (wall-clock) ratios between DG(TD)^2 schemes with optimized TDRK timestepping and the DGTD schemes with SSP-RK timestepping. The second order schemes use TDRK(1, 2)/SSP-RK2 timestepping. The third order schemes use TDRK(2, 3) opt./SSP-RK3 timestepping. The fourth order schemes use TDRK(3, 4) opt./SSP-RK(5, 4) timestepping.

Zones	DG P = 1, $T_{DGTD}/T_{DG(TD)2}$	DG P = 2, $T_{DGTD}/T_{DG(TD)2}$	DG P = 3, $T_{DGTD}/T_{DG(TD)2}$
8^2	1.00	1.36	1.61
16^2	1.31	1.58	1.53
32^2	1.29	1.29	1.44
64^2	1.19	1.66	1.53
128^2	1.51	1.34	1.29
256^2	1.85	1.58	1.52
512^2	1.42	1.66	1.45

three rows) in Table 15 of Balsara and Käppeli [18]. Here also we observe that the DG(TD)^2 schemes enjoy improved energy preservation properties especially at low resolution. However, please note that the quadratic energy preservation for the DG schemes in Balsara and Käppeli [18] was already quite excellent; so the present DG(TD)^2 schemes improve on an already salutary situation.

In order to illustrate the computational advantage of the presented DG(TD)^2 schemes, we present runtime (wall-clock) ratios between the new schemes and the DGTD with SSP-RK timestepping schemes from Balsara and Käppeli [18]. The runtimes were measured on identical machines of the EULER cluster at ETHZ. Moreover, all schemes were implemented within the same computer code in order to avoid (as much as possible) any systematic bias stemming from software design and implementation. The results are displayed in Table 6. We note that the DG(TD)^2 schemes show a substantial increase in computational efficiency on the considered simple test problem.

7. Conclusions

In this paper we have achieved three main goals applied to CED. First, we have shown how the recent globally constraint-preserving DG schemes by Balsara and Käppeli [14], [18] can be meld together with two recent advances. The first advance is the recently developed multidimensional Generalized Riemann Problem (GRP) solver for CED by Balsara et al. [20]. The second advance is the use of Two-Derivative Runge-Kutta (TDRK) timestepping. The resulting schemes have been named DG(TD)^2, where the first "TD" stands for Time-Derivative and the second "TD" for TDRK timestepping. We have thoroughly described the novel schemes in a two-dimensional Cartesian setting. Second, we have used the free parameters in TDRK timestepping to achieve uniformly large CFL with increasing order of accuracy while minimizing the dissipation and dispersion errors. And thirdly, we have documented the von Neumann stability analysis of the DG(TD)^2 schemes and quantified in detail their dissipation and dispersion properties.

At second order we find a DG(TD)^2 scheme with CFL of 0.25 and improved dissipation and dispersion properties; for a second order scheme. At third order we present a novel DG(TD)^2 scheme with CFL of 0.2571 and improved dissipation and dispersion properties; for a third order scheme. At fourth order we find a DG(TD)^2 scheme with CFL of 0.2322 and improved dissipation and dispersion properties. As an extra benefit, the resulting DG(TD)^2 schemes for CED require fewer synchronization steps on parallel supercomputers than comparable DGTD schemes for CED. We also document some test problems to show that the methods achieve their design accuracy. The new DG(TD)^2 schemes also show excellent preservation of quadratic electromagnetic energy on the computational mesh.

It would be interesting to combine the present approach to classical RKDG schemes without constraint-preserving properties, as used e.g. in Computational Fluid Dynamics for the Euler or Navier-Stokes equations. In principle, the combination of a (multidimensional) GRP solver together TDRK timestepping could lead to similar improvements of the CFL stability constraint. However, this is beyond the scope of the present paper and will be dealt with in a forthcoming publication.

Declaration of competing interest

The authors declare that they have no known competing financial interests or personal relationships that could have appeared to influence the work reported in this paper.

Acknowledgements

DSB acknowledges support via NSF grants NSF-ACI-1533850, NSF-DMS-1622457, NSF-ACI-1713765 and NSF-DMS-1821242. Computer support on NSF's Blue Waters computing resources is also acknowledged. RK acknowledges support by the Swiss National Science Foundation (SNSF) under grant 200021-169631. The authors acknowledge the computational resources provided by the EULER cluster of ETHZ. PC would like to acknowledge support from the MATRICS project (MTR/2018/000006) of SERB-DST, India.

References

[1] L.D. Angulo, J. Alvarez, M.F. Pantoja, S.G. Garcia, A.R. Bretones, Discontinuous Galerkin Time Domain Methods in Computational Electrodynamics: State of the Art, Forum for Electromagnetic Research Methods and Application Technologies (FERMAT).
[2] D.S. Balsara, Divergence-free adaptive mesh refinement for magnetohydrodynamics, J. Comput. Phys. 174 (2001) 614–648.
[3] D.S. Balsara, Second-order-accurate schemes for magnetohydrodynamics with divergence-free reconstruction, Astrophys. J. Suppl. Ser. 151 (2004) 149–184.
[4] D.S. Balsara, Divergence-free reconstruction of magnetic fields and WENO schemes for magnetohydrodynamics, J. Comput. Phys. 228 (2009) 5040–5056.
[5] D.S. Balsara, Multidimensional HLLE Riemann solver; application to Euler and magnetohydrodynamic flows, J. Comput. Phys. 229 (2010) 1970–1993.
[6] D.S. Balsara, A two-dimensional HLLC Riemann solver for conservation laws: application to Euler and magnetohydrodynamic flows, J. Comput. Phys. 231 (2012) 7476–7503.
[7] D.S. Balsara, M. Dumbser, R. Abgrall, Multidimensional HLL and HLLC Riemann solvers for unstructured meshes – with application to Euler and MHD flows, J. Comput. Phys. 261 (2014) 172–208.
[8] D.S. Balsara, Multidimensional Riemann problem with self-similar internal structure – Part I – application to hyperbolic conservation laws on structured meshes, J. Comput. Phys. 277 (2014) 163–200.
[9] D.S. Balsara, M. Dumbser, Divergence-free MHD on unstructured meshes using high order finite volume schemes based on multidimensional Riemann solvers, J. Comput. Phys. 299 (2015) 687–715.
[10] D.S. Balsara, M. Dumbser, Multidimensional Riemann problem with self-similar internal structure – Part II – application to hyperbolic conservation laws on unstructured meshes, J. Comput. Phys. 287 (2015) 269–292.
[11] D.S. Balsara, Three dimensional HLL Riemann solver for structured meshes; application to Euler and MHD flow, J. Comput. Phys. 295 (2015) 1–23.
[12] D.S. Balsara, J. Vides, K. Gurski, B. Nkonga, M. Dumbser, S. Garain, E. Audit, A two-dimensional Riemann solver with self-similar sub-structure – alternative formulation based on least squares projection, J. Comput. Phys. 304 (2016) 138–161.
[13] D.S. Balsara, T. Amano, S. Garain, J. Kim, High order accuracy divergence-free scheme for the electrodynamics of relativistic plasmas with multidimensional Riemann solvers, J. Comput. Phys. 318 (2016) 169–200.
[14] D.S. Balsara, R. Käppeli, von Neumann stability analysis of globally divergence-free RKDG and PNPM schemes for the induction equation using multidimensional Riemann solvers, J. Comput. Phys. 336 (2017) 104–127.
[15] D.S. Balsara, A. Taflove, S. Garain, G. Montecinos, Computational electrodynamics in material media with constraint-preservation, multidimensional Riemann solvers and sub-cell resolution – Part I, second-order FVTD schemes, J. Comput. Phys. 349 (2017) 604–635.
[16] D.S. Balsara, A. Taflove, S. Garain, G. Montecinos, Computational electrodynamics in material media with constraint-preservation, multidimensional Riemann solvers and sub-cell resolution – Part II, higher-order FVTD schemes, J. Comput. Phys. 354 (2018) 613–645.
[17] D.S. Balsara, B. Nkonga, Formulating multidimensional Riemann solvers in similarity variables – Part III: a multidimensional analogue of the HLLI Riemann solver for conservative hyperbolic systems, J. Comput. Phys. 346 (2017) 25–48.
[18] D.S. Balsara, R. Käppeli, von Neumann stability analysis of globally constraint-preserving DGTD and PNPM schemes for the Maxwell equations using multidimensional Riemann solvers, J. Comput. Phys. 376 (2019) 1108–1137.
[19] D.S. Balsara, J. Li, G. Montecinos, An efficient, second order accurate, universal generalized Riemann problem solver based on the HLLI Riemann solver, J. Comput. Phys. 375 (2018) 1238–1269.
[20] D.S. Balsara, A. Hazra, S. Garain, P. Chandrashekar, Multidimensional generalized Riemann problem solver for Maxwell's equations, J. Comput. Phys. (2019), submitted for publication.
[21] A. Barbas, P. Velarde, Development of a Godunov method for Maxwell's equations with adaptive mesh refinement, J. Comput. Phys. 300 (2016) 186–201.
[22] V. Bokil, Y. Chang, Y. Jiang, F. Li, Energy stable discontinuous Galerkin methods for Maxwell's equations in nonlinear optical media, J. Comput. Phys. 350 (2017) 420–452.
[23] R.P.K. Chan, A.Y.J. Tsai, On explicit two-derivative Runge-Kutta methods, Numer. Algorithms 53 (2010) 171–194.
[24] J. Chen, Q.H. Liu, Discontinuous Galerkin time-domain methods for multiscale electromagnetic simulations: a review, Proc. IEEE 101 (2) (2013) 242–254.
[25] B. Cockburn, C.-W. Shu, TVB Runge-Kutta local projection discontinuous Galerkin finite element method for conservation laws II: general framework, Math. Comput. 52 (1989) 411–435.
[26] B. Cockburn, S. Hou, C.-W. Shu, TVB Runge-Kutta local projection discontinuous Galerkin finite element method for conservation laws IV: the multidimensional case, J. Comput. Phys. 54 (1990) 545–581.
[27] B. Cockburn, C.-W. Shu, The Runge-Kutta discontinuous Galerkin method for conservation laws V: multidimensional systems, J. Comput. Phys. 141 (1998) 199–224.
[28] B. Cockburn, C.-W. Shu, Runge-Kutta discontinuous Galerkin methods for convection dominated problems, J. Sci. Comput. 16 (2001) 173–261.
[29] B. Cockburn, F. Li, C.-W. Shu, Locally discontinuous Galerkin methods for the Maxwell equations, J. Comput. Phys. 194 (2004) 588–610.
[30] R. Diehl, K. Busch, J. Niegemann, Comparison of low-storage Runge-Kutta schemes for discontinuous Galerkin time-domain simulations of Maxwell's equations, J. Comput. Theor. Nanosci. 7 (8) (2010) 1572–1580.
[31] M. Dumbser, D.S. Balsara, E.F. Toro, C.-D. Munz, A unified framework for the construction of quadrature-free one-step finite-volume and discontinuous Galerkin schemes, J. Comput. Phys. 227 (2008) 8209–8253.
[32] H. Egger, F. Kretzschmar, S.M. Schnepp, I. Tsukerman, T. Weiland, Transparent boundary conditions for a discontinuous Galerkin Trefftz method, Appl. Math. Comput. 267 (2015) 42–55.
[33] C.R. Goetz, D.S. Balsara, M. Dumbser, A family of HLL-type solvers for the generalized Riemann problem, Comput. Fluids 169 (2018) 201–212.
[34] S. Gottlieb, C.-W. Shu, E. Tadmor, Strong stability-preserving higher order time discretization methods, SIAM Rev. 43 (1) (2001) 89–112.
[35] Z. Grant, S. Gottlieb, D.C. Seal, A Strong Stability Preserving Analysis for Multistage Two-Derivative Time-Stepping Schemes Based on Taylor Series Conditions, arXiv:1804.10526v1.
[36] A. Hazra, P. Chandrashekar, D.S. Balsara, Globally constraint-preserving FR/DG scheme for Maxwell's equations at all orders, J. Comput. Phys. (2019), in press.
[37] J. Hesthaven, T. Warburton, Nodal high-order methods on unstructured grids, I: time-domain solution of Maxwell's equations, J. Comput. Phys. 181 (2002) 186–221.

[38] J.S. Hesthaven, T. Warburton, Nodal Discontinuous Galerkin Methods: Algorithms, Analysis, and Applications, 1st ed., Springer Publishing Company, Incorporated, 2007.
[39] T.Z. Ismagilov, Second order finite volume scheme for Maxwell's equations with discontinuous electromagnetic properties on unstructured meshes, J. Comput. Phys. 282 (2015) 33–42.
[40] F. Kretzschmar, S.M. Schnepp, I. Tsukerman, T. Weiland, Discontinuous Galerkin methods with Trefftz approximations, J. Comput. Appl. Math. 270 (2014) 211–222.
[41] S.G. Johnson, The NLopt nonlinear-optimization package, http://github.com/stevengj/nlopt.
[42] Y. Liu, C.-W. Shu, E. Tadmor, M. Zhang, L2 stability analysis of the central discontinuous Galerkin method and comparison between the central and regular discontinuous Galerkin methods, Math. Model. Numer. Anal. 42 (2008) 593–607.
[43] C.-D. Munz, P. Omnes, R. Schneider, E. Sonnendrücker, U. Voß, Divergence correction techniques for Maxwell solvers based on a hyperbolic model, J. Comput. Phys. 161 (2000) 484.
[44] J. Niegemann, R. Diehl, K. Busch, Efficient low-storage Runge–Kutta schemes with optimized stability regions, J. Comput. Phys. 231 (2) (2012) 364–372.
[45] M.J.D. Powell, A Direct Search Optimization Method That Models the Objective and Constraint Functions by Linear Interpolation, Advances in Optimization and Numerical Analysis, Springer, Netherlands, 1994, pp. 51–67.
[46] M.J.D. Powell, Direct Search Algorithms for Optimization Calculations, Acta Numer. 7 (1998) 287–336, Cambridge University Press (CUP).
[47] W.H. Reed, T.R. Hill, Triangular mesh methods for the neutron transport equation, Technical Report LA-UR-73-479, Los Alamos Scientific Laboratory, Los Alamos, 1973.
[48] Q. Ren, Q. Sun, L. Tobón, Q. Zhan, Q.H. Liu, EB scheme-based hybrid SE-FE DGTD method for multiscale EM simulations, IEEE Trans. Antennas Propag. 64 (9) (2017) 4088–4091.
[49] D. Sarmany, M.A. Botchev, J.J. Vegt, Dispersion and dissipation error in high-order Runge-Kutta discontinuous Galerkin discretisations of the Maxwell equations, J. Sci. Comput. 33 (2007) 47–74.
[50] R.J. Spiteri, S.J. Ruuth, A new class of optimal high-order strong-stability-preserving time-stepping schemes, SIAM J. Numer. Anal. 40 (2002) 469–491.
[51] R.J. Spiteri, S.J. Ruuth, Non-linear evolution using optimal fourth-order strong-stability-preserving Runge-Kutta methods, Math. Comput. Simul. 62 (2003) 125–135.
[52] C.-W. Shu, S.J. Osher, Efficient implementation of essentially non-oscillatory shock capturing schemes, J. Comput. Phys. 77 (1988) 439–471.
[53] C.-W. Shu, S.J. Osher, Efficient implementation of essentially non-oscillatory shock capturing schemes II, J. Comput. Phys. 83 (1989) 32–78.
[54] C.-W. Shu, Total variation-diminishing time discretizations, SIAM J. Sci. Stat. Comput. 9 (1988) 1073–1084.
[55] Q. Sun, R. Zhang, Q. Zhan, Q.H. Liu, A novel coupling algorithm for perfectly matched layer with wave equation-based discontinuous Galerkin time-domain method, IEEE Trans. Antennas Propag. 66 (1) (2018) 255–261.
[56] A. Taflove, Review of the formulation and applications of the finite-difference time-domain method for numerical modeling of electromagnetic wave interactions with arbitrary structures, Wave Motion 10 (1988) 547–582.
[57] A. Taflove, S. Hagness, Computational Electrodynamics, third edition, Artech House, 2005.
[58] A. Taflove, A. Oskooi, S. Johnson, Advances in FDTD Computational Electrodynamics – Photonics and Nanotechnology, Artech House, 2013.
[59] A. Taflove, S. Hagness, Finite difference time domain solution of Maxwell's equations, WEEEE Rev. (2016) 8303.
[60] H. Wang, L. Xu, B. Li, S. Descombes, S. Lantéri, A new family of exponential-based high-order DGTD methods for modeling 3-D transient multiscale electromagnetic problems, IEEE Trans. Antennas Propag. 65 (11) (2017) 5960–5974.
[61] J.H. Williamson, Low-storage Runge-Kutta schemes, J. Comput. Phys. 35 (1) (1980) 48–56.
[62] K.S. Yee, Numerical solution of initial boundary value problems involving Maxwell equation in an isotropic media, IEEE Trans. Antennas Propag. 14 (1966) 302.
[63] Z. Xu, D.S. Balsara, H. Du, Divergence-free WENO reconstruction-based finite volume scheme for ideal MHD equations on triangular meshes, Commun. Comput. Phys. 19 (04) (2016) 841–880.
[64] H. Yang, F. Li, Stability analysis and error estimates of an exactly divergence-free method for the magnetic induction equations, Modél. Math. Anal. Numér. 50 (4) (2016) 965–993.
[65] M. Zhang, C.-W. Shu, An analysis of and a comparison between the discontinuous Galerkin and the spectral finite volume methods, Comput. Fluids 34 (2005) 581–592.